NTNU
Norwegian University of
Science and Technology

C-TiB_2 Composite Inert Cathode Material by Spark Plasma Sintering

Audun Håberg

Chemical Engineering and Biotechnology
Submission date: August 2018
Supervisor: Zhaohui Wang, IMA
Co-supervisor: Tor Grande, IMA
Mari-Ann Einarsrud, IMA
Samuel Senanu, IMA

Norwegian University of Science and Technology
Department of Materials Science and Engineering

Preface

This studies in this master thesis has been carried out at the Department of Material Science and Engineering, Norwegian University of Science and Technology (NTNU), Trondheim, spring 2018, with Zhaohui Wang as main supervisor and with co-supervisors Tor Grande, Mari-Ann Einarsrud and Samuel Senanu.

This master thesis is a continuation of the a project report "C-TiB_2 Composite Inert Cathode Material by Spark Plasma Sintering - Spark Plasma Sintering of TiB_2" from the fall of 2017, by the same author. The introduction and the section on the sintering of TiB_2 from the project report, is reused in this work with some modifications.

Abstract

TiB_2 has been considered a potential inert, wettable cathode material for aluminum reduction cells for a long time. An important characteristic of TiB_2 as a cathode material, is its excellent wetting properties towards molten aluminium. Because of the high cost and poor machining properties of TiB_2, composites of C-TiB_2 has been suggested as an alternative cathode material. In this work, nine C-TiB_2 composites ranging from pure TiB_2 to 85 wt% C were successfully sintered using Spark Plasma Sintering. Almost theoretical density of pure TiB_2 was obtained with 97.1% relative density. Composites with 15 wt% C and 25 wt% C were sintered with relative high relative density of 91.3% and 79.8% respectively. The relative density of the composites ranging from 35 wt% C to 85 wt% C, were limited to just above 60%. The Sessile Drop method was used to test the wetting behaviour of molten aluminium on the sintered composites, including tests on pure TiB_2 and graphite. Equilibrium contact angles were reached at 1100 °C for three samples including pure TiB_2, composite with 15 wt% C and graphite at 9.1°, 22.2° and 11.6° respectively. No stable contact angle were reached for the remaining composites. The dependence of carbon composition on the wetting angles were not discerned from the current measurements. The plausible reason and dynamic wetting behaviour at elevated temperatures were elaborated.

Sammendrag

TiB_2 har blitt betraktet som et potensielt inert, fuktende katodemateriale for aluminium-sreduksjonsceller i lang tid. En viktig egenskap til TiB_2 er dets gode fuktingsegenskaper mot smeltet aluminium. På grunn av høye kostnader og dårlige bearbeidnings egenskaper til TiB_2, har et kompositt av C-TiB_2 blitt foreslått som en et alternativt katodemateriale. I dette arbeider har ni C-TiB_2 kompositter, som strekker seg fra ren TiB_2 til 85 wt% C, blitt sintret ved bruk av Spark Plasma Sintring. Nesten teoretisk tetthet ble oppnådd for ren TiB_2 med 97.1% relativ tetthet. Kompositter med 15 wt% C og 25 wt% C ble sintret med relativ høy relativ tetthet på henholdsvis 91.3% og 79.8%. Den relative tettheten av de resterende kompositten fra 35 wt% C til 85wt% C, var begrenset til rett over 60%. Sessile Drop metoden ble bruk til å teste fuktingsegenskapene til smeltet aluminium på de sintrede kompositten, inkludert tester på ren TiB_2 og grafitt. Likevektskontaktvinkler ble nådd på 1100 °C for tre prøver, inkludert ren TiB_2, kompositt med 15 wt% C og grafitt på henholdsvis 9.1°, 22.2° og 11.6°. Ingen stabil kontaktvinkel ble nådd for de resterende kompositten. Det ble ikke observert noen tilsynelatende sammenheng mellom karbon-komposisjonen og fuktingsoppførslene for de forskjellige kompositten. Mulige årsaker for dette og den dynamiske fuktingsoppførslene ved høyere temperaturer ble utdypet.

Acknowledgment

First and foremost, I wish to thank my supervisor, Zhaohui Wang for her time, guidance and support. I would also like to thank my co-supervisors Tor Grande and Samuel Senanu for useful tips on how to proceed with my work and Mari-Ann Einarsrud with helping me interpret sintering data. An extra thanks to Sarina Bao, for helping me with with the Sessile Drop equipment and giving me useful information on wetting. Also thanks to Dmitry Slizovskiy, for helping me with Spark Plasma Sintering.

Contents

List of Figures

List of Tables

1. Introduction

1.1 Background

Aluminium is a very important metal in todays society and is counted as the second most important metal, after iron [1]. It is the third most abundant element in the world and in 2016 a total of 60 million metric tonnes of aluminium was produced worldwide [2]. Charles Martin Hall and Paul Héroult revolutionized the aluminium production after individually inventing the Hall-Héroult process for producing aluminium in the late 19th century [3]. This has been the dominant aluminium production process ever since. Over the years there has been much development of the process, but the main process remains unchanged. In the process, alumina (Al_2O_3) is dissolved in molten cryolite where it is reduced to aluminium metal. The overall electrochemical reaction can be written as:

$$Al_2O_3(\text{dissolved}) + \frac{3}{2}C(s) \longrightarrow 2\,Al(l) + \frac{3}{2}CO_2(g) \tag{1.1}$$

The required power consumption for producing aluminium using the Hall-Héroult process has been reduced significantly over the years, but there is still a considerable difference between the theoretically possible power consumption (6.45 kWh/kg Al at 970 °C) and actual power consumption (close to 14kWh/kg Al) [4]. Because of this, the aluminium industry is still trying to improve the efficiency of the aluminium production by reducing the power consumption.

The main components of the alumina reduction cell used today is sketched in Figure 1.1.

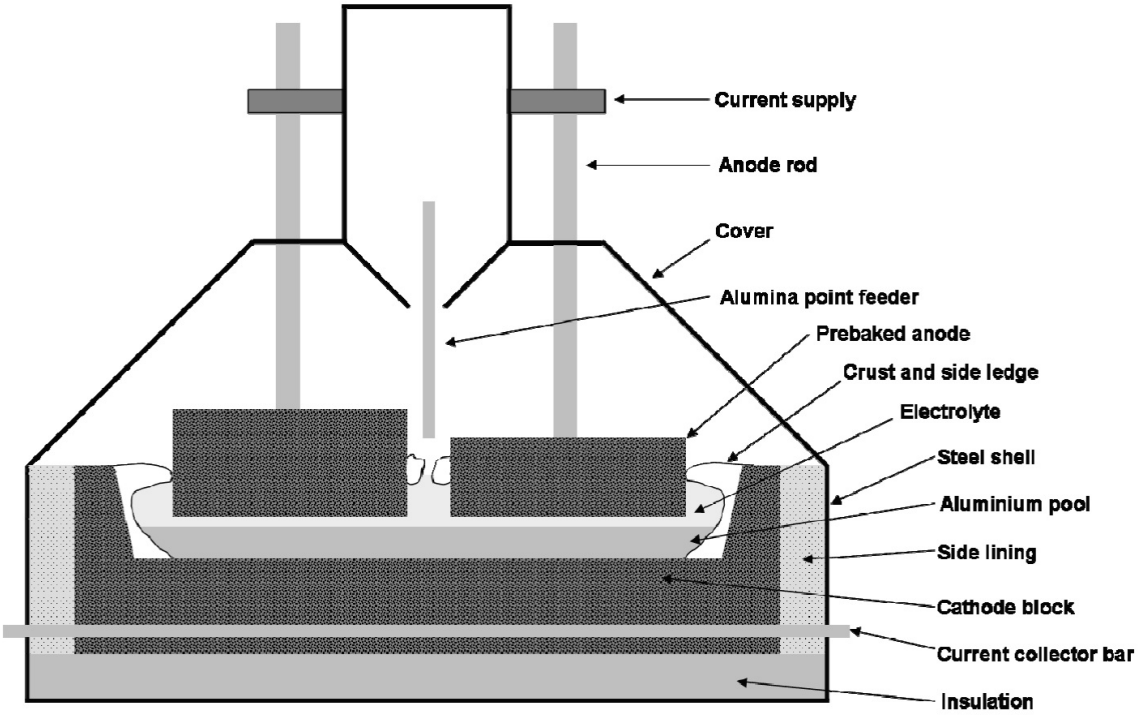

Figure 1.1: A sketch of the components included in the Hall-Héroult alumina reduction cell. Extracted from [4].

The cathode block made of carbon materials wets the molten aluminium very poorly. As a result of this, a thick layer of aluminium is required in order to cover the cathode. In the presence of strong magnetic field during operation, magneto- hydrodynamic disturbances is induced in the aluminium causing movement in the metal. To prevent contact between the metal and the anode, which will lead to short circuit, additional distance between the two electrodes are required. This extra distance between the electrode results in a considerable ohmic voltage drop in the electrolyte which represents between 30-40% of the energy consumption of the process [5].

In order to reduce such ohmic voltage drop, an alternative cell design has been proposed. This alternative alumina reduction cell design is the drained cell illustrated in Figure 1.2.

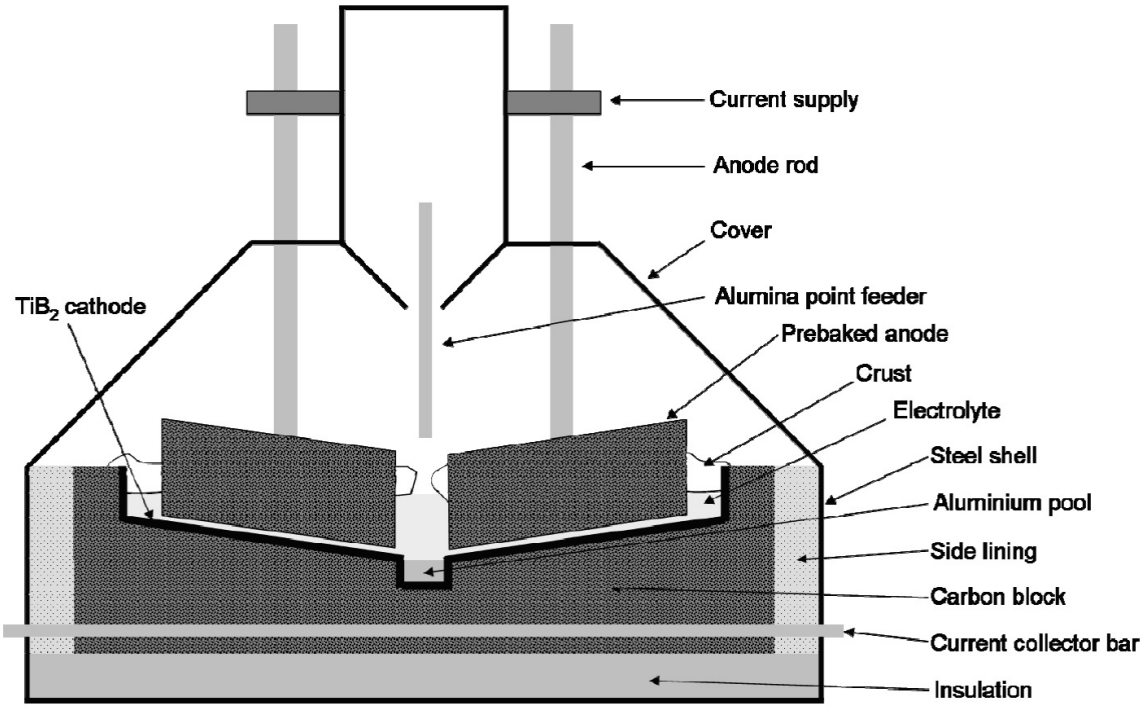

Figure 1.2: A sketch of the components included in the Hall-Héroult alumina reduction cell with a drained cathode. Extracted from [4].

This cell is designed to minimize the distance needed between the aluminium and the anodes so that the energy consumption can be reduced dramatically. In order for this cell to work, the cathode lining need to wet the aluminium sufficiently enough for the aluminium to make a thin film on the lining. Some other important properties needed for the cathode lining in this cell are high electric conductivity, sufficient mechanical strength and stability towards thermal stresses and good chemical resistance towards both the aluminium and the electrolyte. Due to its chemical and physical properties TiB_2 has been the most promising candidate as this cathode lining material for a many years [4]. Some drawbacks with TiB_2 is that it has a very high price and has very poor machining properties. Making a composite material of TiB_2 and Carbon has been suggested as a possible solution to reduce the cost of the material while still keeping the good properties as a cathode lining material.

1.2 Aim of the Work

The aim of this work is two fold. The first is to is sinter the dense TiB_2 material (project work) and the low cost, dense C-TiB_2 composite material. The second is to check the wetting properties of the sintered materials to find out if the composite materials can still maintain the desired properties, namely good wetting towards molten aluminum. Moreover, the dependence of wetting properties with respect to the amount of carbon content in the composites, can be studied. The composites will be sintered with Spark Plasma Sintering (SPS) using different carbon content. The wetting properties of the composites will be measured using Sessile Drop method.

2. Literature Review

This chapter consists of three main parts. The first part will give a presentation of TiB_2 and its properties. In the second part, a basis to understand sintering will be provided with an introduction to the Spark Plasma Sintering method. Following that, the sintering of TiB_2 and the effect of carbon addition will be presented. In the third part, a basis to understand wetting will be provided with an introduction to the Sessile Drop method. Furthermore, the wetting of TiB_2 and C with molten Al will be presented.

2.1 Titanium Diboride

Titanium Diboride (TiB_2) is an extremely hard ceramic with excellent wetting properties towards molten aluminium [4]. It is part of the binary metal borides group, and has many of the typical characteristics of a boride:

- **High melting point**. There are a wide range of reported values for the melting point of TiB_2, ranging from 2700 °C to 3300 °C. The most accepted value for the melting point is 3225 °C [6].
- **High thermal conductivity**. The thermal conductivity of TiB_2 is particularly high with value close to 100 W/mK. Excellent thermal shock resistance is a result of this high thermal conductivity [4].
- **High electrical conductivity**. TiB_2 has a low resistivity at around 9 $\mu\Omega cm^2$ which is dependant on impurity level, temperature and the density of the material [4] .

- **High chemical stability**. TiB_2 is particularly resistant towards several molten salts, liquid metals and acidic slags [4].

Table 2.1 list most of the physical and mechanical properties of TiB_2 mentioned. As was mention in section 1.1, most of these physical and chemical properties makes TiB_2 well suited as a cathode lining material. The excellent wetting properties towards molten aluminium, which is the most important property for this research, will be presented in Section 2.3.5.

Table 2.1: Some physical and mechanical properties of TiB_2. Extracted from [4].

Property	**Value**
Density	4.52 g/cm^3
Melting Point	3225 °C
Hardness	25 GPa
Flexual strength	400 MPa
Electric resistance	9 μΩcm^2
Thermal conductivity	96 W/mK
Thermal expansion (293K)	7.4×10^{-6} K^{-1}

The crystal structure of TiB_2 has an AlB_2 structure of the space group P6/mmm. The structure is shown in Figure 2.1.

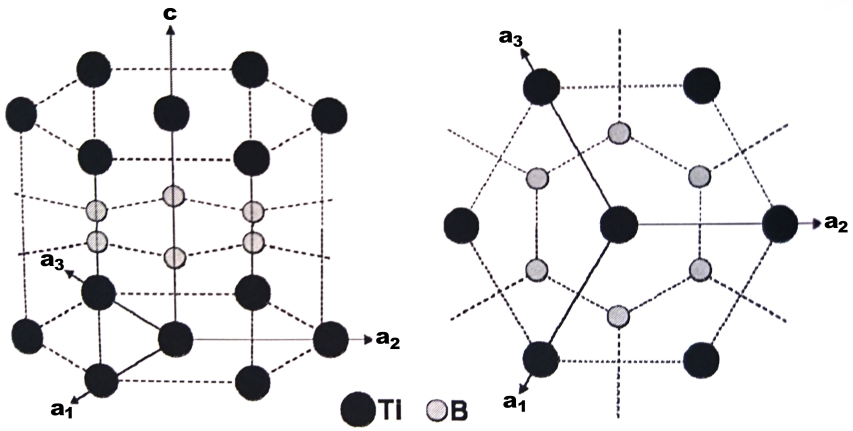

Figure 2.1: The AlB_2 structure of TiB_2. Perspective view on the left and projection along the c-axis on the right. Extracted from [4].

The unit cell is hexagonal with the lattice parameters a=3.028 Å and c=3.228 Å at room

temperature [7]. Thermal expansion is different for the a-axis and c-axis which results in anisotropic thermal expansion behaviour.

Some mentioned drawbacks with TiB_2 are the high cost of the material and poor machining properties. Rapid degradation of the bulk material, mainly due to aluminium penetration along the grain boundaries, has also been reported [8]. These are drawbacks that needs to be addressed if TiB_2 is to be an economically viable industrial cathode lining material.

2.2 Sintering

This section will provide the basis to understand sintering and give an introduction to the Spark Plasma Sintering method. Following that, the sintering of TiB_2 and the effect of carbon addition will be presented.

2.2.1 Basis of Sintering

Sintering of a ceramic powder is the densification of the powder to form a compact, dense solid structure by heat treatment. Sintering is by Richerson [9] described essentially as removal of the pores between the particles combined with growth together and strong bonding between adjacent particles. For sintering to occur it requires a mechanism for material transport to be present and it needs a source of energy to activate and sustain this material transport. Reduction in the Gibbs energy for the system due to the reduction of surface area of the powder particles, is the macroscopic driving force for the sintering process. The driving force at micro scale is related to surface curvature and capillary forces. Figure 2.2 illustrates several of the material transport mechanisms that can take place during sintering [4].

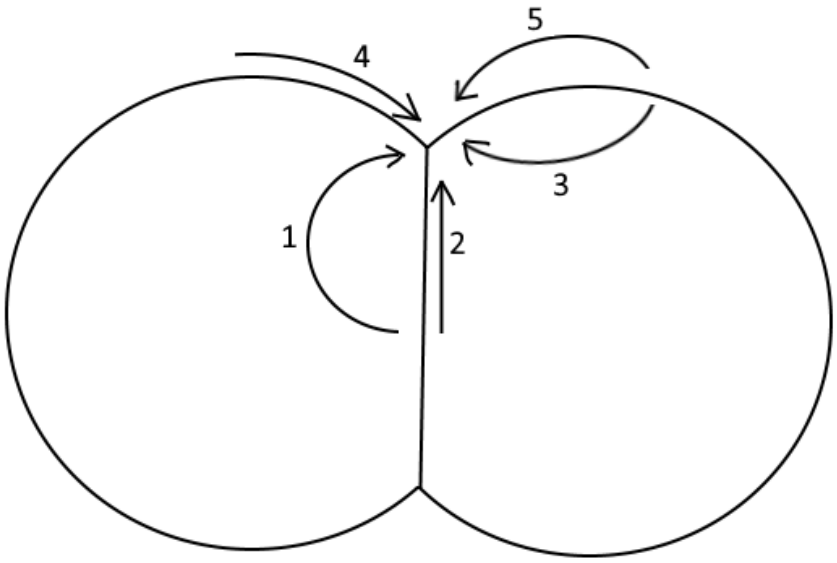

Figure 2.2: Illustration of the mass transport mechanisms between two particles during sintering. 1 represents volume diffusion from grain boundary, 2 represents grain boundary diffusion, 3 represents volume diffusion from surface, 4 represents surface diffusion and 5 represents evarporation-condensation. The figure is based on a figure in [4].

The centers of the particles, approach each other during sintering as an effect of the grain boundary diffusion and the volume diffusion along the grain boundary, thus promoting densification. The centers of the particles does not approach each other during surface diffusion, evaporation-condensation and volume diffusion from the surface. However, the surface area is still reduced which results in coarsening of the material [4].

To simplify the process, sintering can be divided into three main stages by observations of the physical changes to the material as particles bond and the pores between the particles are reduced. The three stages, starting from loose powder, are illustrated in Figure 2.3. The three stages are [9]:

- **Initial stage**: The particles are rearranged and initial formation of contact points called neck formation takes place.

- **Intermediate stage**: The size of the necks between the adjacent particles grows and grain boundaries are formed. The centers of the original particles move closer to each other and porosity decreases. This stage results in most of the densification during sintering. The intermediate sintering ends when the pores are closed and no longer can

hinder grain growth.

- **Final stage**: Grain growth occurs and the material reaches its final density. The pores are removed by controlled grain growth and by movement of the grain boundaries.

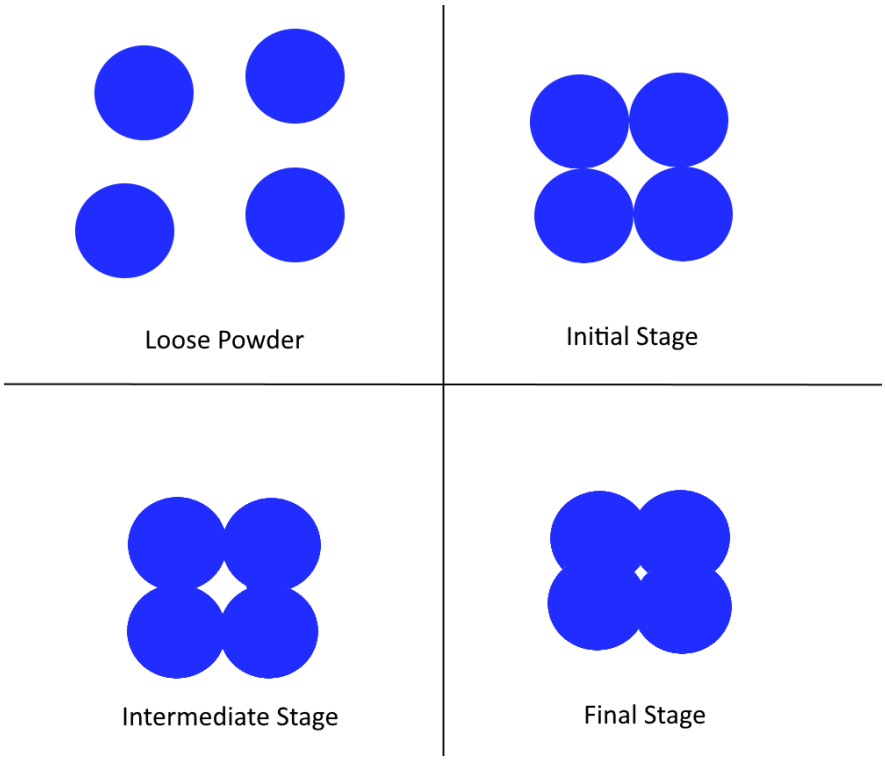

Figure 2.3: Illustration of the stages of sintering where the blue circles represents powder particles. Based on a figure from [10]

2.2.2 Spark Plasma Sintering

Spark plasma sintering (SPS) is a relatively new sintering technique using uniaxial pressure and a pulsing electrical current (DC current) to perform high speed consolidation of the powder. The current goes through a graphite die with graphite pistons and through the powder. The heating power is distributed homogeneously over the volume of the powder compact in the microscopic scale, but is dissipated exactly where the energy is required for the sintering process in the microscopic scale, which is at the contact point between adjacent powder particles. The energy dissipation is illustrated in Figure 2.4. This way of heating up the powder results in favourable sintering behaviour with suppressed powder decomposition and less grain growth [11].

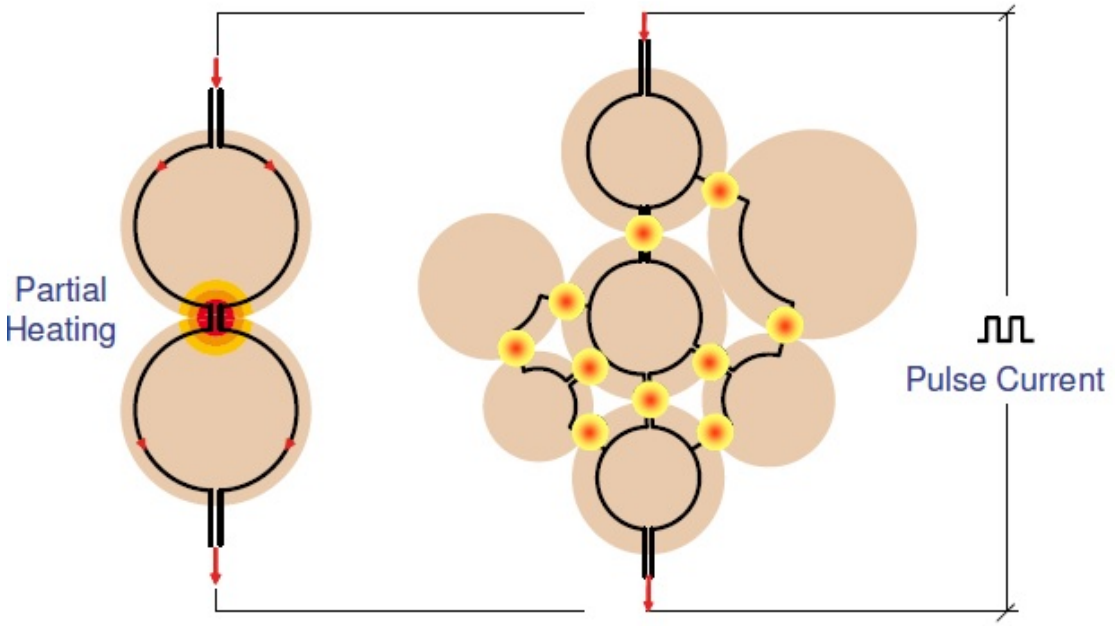

Figure 2.4: Illustration of energy dissipation in the microscopic scale. The black lines represents the path of the pulse current and the red dots between particles indicates partial heating. Extracted from [11].

SPS has many advantages to other sintering techniques. This includes high sintering speed, high reproducibility, reliability and safety, ease of operation and accurate control of the sintering energy. Heating rates as high as 1000 °C/min can be achieved. This is dependent on the electric power supply, the electrical and thermal properties of the sample and on the geometry of container/sample. The rapid heating rate can reduce the time needed for sintering significantly compared to other sintering techniques such as Hot Pressing (HP). Both temperature and pressure are applied simultaneously, which can result in a lower sintering temperature compared to pressure-less sintering. Using SPS, the sintering temperatures can be lowered as much as 200 °C to 500 °C compared to conventional sintering [11]. A combination of the reduced sintering temperature and the dissipation of energy at the contact points, makes SPS capable of sintering diffcult-to-sinter materials such as hafnium diboride and tungsten carbide without the use of sintering aids [12]. Furthermore, the lower sintering temperatures and lower time required makes it possible to achieve close to theoretical values with little grain growth using nanometric powders [13].

Many efforts have been made in investigation of the SPS process. For the SPS of powders, Zhang et al. [14] proposed that the sintering process could be divided into the following four stages:

1. Activation and refining of the powder
2. Formation and growth of the sintering neck
3. Rapid densification
4. Plastic deformation densification

Stage one and two are both promoted by spark discharges between the powder particles illustrated as "partial heating" in Figure 2.4. Spark discharges heats up the powder surface and removes oxides. In the second stage, the neck formation occurs due to diffusion and evaporation/condensation. When the necks are formed, spark discharges will no longer happen between the connected particles. The high density current will pass through the necks instead and result in heating up the material by Joule heating. Joule heating will become the main heating mode when enough necks are formed between the particles. Stage three, rapid densification of the bulk material, will occur because of the increase of the temperature. Stage four is a result of the combination of the high temperature and the axial pressure applied and deformation densification will start when the holding pressure is loaded [14].

Lastly, it should be mentioned that there are a lot of controversy on the existence of spark plasma and the occurrence of discharge during sintering. Here are two examples: By direct visual observations and characteristic microstructure analysis, Zhang et al. [15] concluded that spark discharge occurs during the sintering process. On the other hand, by using ultrafast in situ voltage measurements, in situ atomic emission spectroscopy and direct visual observations, Hulbert et al. [16] concluded that there were no spark discharge occurs during the sintering process.

2.2.3 Sintering of TiB_2

Sintering of TiB_2 is very difficult because of its high melting point, predominant covalent bonding, low self-diffusion coefficient and oxide layer (TiO_2 and B_2O_3) on the powder surface.

Conventional sintering without any additives require sintering temperature up to over 2200 °C [17]. By using SPS or HP, the sintering temperatures can be lowered significantly. Zhang et al. [17] sintered TiB_2 using SPS over a temperature range of 1200-1800 °C. It was shown that sintering started for SPS at a temperature as low as 1400 °C. By using SEM, neck formation between the TiB_2 particles was observed at this temperature. A temperature of 1800 °C was reported to give the densest microstructure in the temperature range used.

As mentioned in section 2.1, TiB_2 has a hexagonal crystal structure which leads to anisotropic thermal expansion. By observation with SEM of TiB_2-based ceramics, a critical grain size has been suggested to be around 15 µm [18]. If the average grain size exceeds the critical grain size during sintering, cracking along the grain boundaries can occur during cooling of the material. Wang et al. [19], prepared samples of TiB_2 with HP at temperatures between 1500 and 1900 °C. It was determined that the grain size in general increased slowly at low temperatures, but increased rapidly at higher temperatures. Zhang et al. [17], reported the same for SPS where rapid grain growth started after 1700 °C with a axial pressure of 50 MPa.

Königshofer et al. [20], demonstrated the dependence of axial pressure of TiB_2-ceramic materials. For this TiB_2 was sintered with HP at a temperature of 1800 °C. By increasing the axial pressure from 15 MPa to 45 MPa the relative density was increased from 84.9% to 99.5%.

Table 2.2 includes parameters and results from previous experiments found in literature. The table only includes the best results with the highest relative density in each case.

Table 2.2: Sintering parameters from previous work

Sintering method	**Powder size** [µm]	**Temperature** [°C]	**Pressure** [MPa]	**Relative Density** [%]	**ref**
SPS	1-2[1]	1800	50	97.6	[17]
SPS	1.2-2.5[2]	2200	35	88.0	[21]
HP	3-6[3]	1800	50	97.5[4]	[22]
SPS	1[5]	1750	20	98.9[6]	[23]
HP	3-6[7]	1800	45	99.5[8]	[20]

[1] From Ningxia Machinery Research Institute, Ningxia, China
[2] From H.C. Starck
[3] From GE advanced Ceramic, Grade HCT-F, Cleveland, OH
[4] With an addition of 2.55 wt% coal tar pitch
[5] From Shanghai ST-nano science and technology Co. Ltd., China
[6] Composite with 15wt% carbon nano tubes.
[7] From Treibacher Industrie AG (TIAG)
[8] With an addition of 0.5 wt% CrB_2

The Effect of Carbon on Sintering of TiB_2

Oxide impurities in the TiB_2 powder has a limiting effect on the densification during sintering [24]. An addition of carbon to the TiB_2 powder before sintering, can enhance the density of the sintered material. This is due to carbothermal reduction of the oxide impurities according to the following chemical equation:

$$TiO_2(s) + B_2O_3(g) + 5\,C(s) = 5\,CO(g) + TiB_2(s) \tag{2.1}$$

The increase in density has been shown to correspond to the amount of oxygen impurities in the TiB_2 powder. Further increase in the carbon content results in residual carbon and a lower density of the sintered sample. Carbon content has also been shown to prevent exaggerated grain growth during sintering [22] . The increase in density of TiB_2 with a small addition of carbon was also confirmed during the project work [25]. Sintering without carbon addition showed better densification along the edges of the sintered samples, which was attributed to the sintering taking place in a graphite environment.

2.3 Wetting of TiB_2 and C with Molten Al

This section will provide the basis to understand wetting and give an introduction to the Sessile Drop method. Following this, the wetting of TiB_2 and C with molten Al will be presented.

2.3.1 Basis of Wetting

The wettability of a fluid on a solid is the ability of the fluid to maintain contact with the solid surface. Figure 2.5 shows the case where there is contact between three phases (solid, liquid and gas). This results in the three interfaces with three corresponding surface tensions.

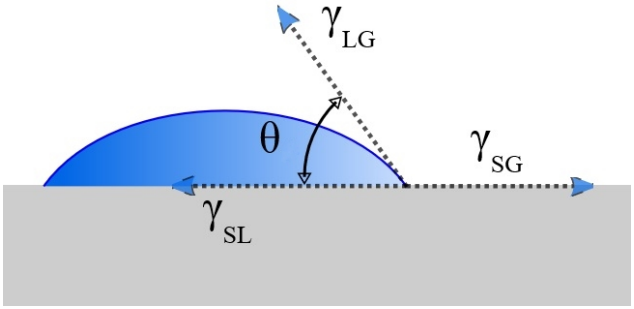

Figure 2.5: The contact angle (θ) of a liquid droplet on a substrate. The three surface tensions from different interfaces are surface tension between solid and liquid (γ_{SL}), surface tension between liquid and gas (γ_{LG}) and surface tension between solid and gas (γ_{SG}). Extracted from [26]

The angle between the solid-liquid interface and the liquid-vapor interface quantifies the wettability of the solid surface by the liquid. It is called the contact angle (θ) and can be calculated using the three surface tensions using Young's equation [26]:

$$cos(\theta) = \frac{\gamma_{SG} - \gamma_{SL}}{\gamma_{LG}} \tag{2.2}$$

There are three different cases of wetting based on the range of the contact angle. These are called **wetting**, **neutral wetting** and **non-wetting** and are illustrated in Figure 2.6 [27].

- **Wetting**: It is wetting when the contact angle is lower than 90°.

- **Neutral wetting**: It is neutral wetting if the contact angle is equal to 90°.
- **Non-wetting**: It is non-wetting when the contact angle is higher than 90°.

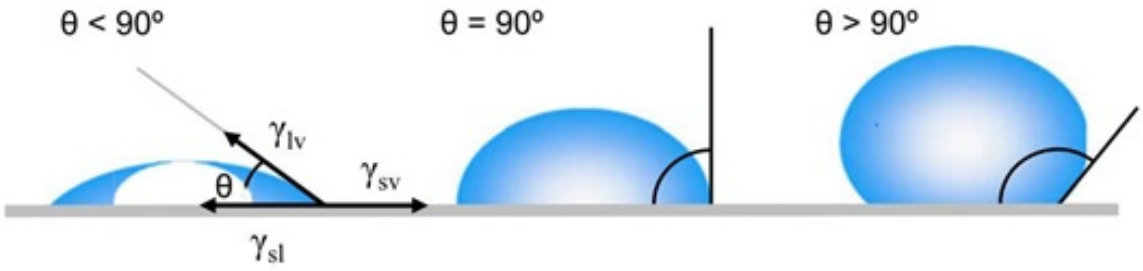

Figure 2.6: Contact angle of the three different wetting cases from left to right: **wetting**, **neutral wetting** and **non-wetting**. Extracted from [28].

2.3.2 Sessile Drop Method

One method to measure wettability, is the Sessile Drop Method. The method is based on visual observation of the contact angle between a melted drop (sessile drop) and a substrate of desired materials [29]. A sample placed on a substrate is heated up in a vacuum or in an inert atmosphere. When the sample melts, the contact angle can be observed and measured. The setup for the experimental apparatus is illustrated and explained in section 3.2.5. To clarify, the "sample" used for wetting is not the same as the "sintered sample" in the sintering section. The sintered material (sintered sample) is the substrate in this case.

When the conducting a Sessile Drop experiment, there are many factors that influences the wetting that must be considered. Firstly, the wetting is time dependant, thus the measured contact angle will change over time. How much and in what manner the contact angle changes, is dependant on the materials properties and the stability of the substrate material in contact with the liquid sample to be tested. It is therefore necessary to understand the materials reactions in the conditions set during operation in order to determine the final contact angles. There are several factors that can affect the wetting properties measured in addition to the different material reactions and the time dependency. Roughness is one of these factors, but the effect that roughness has on the wetting can be difficult to determine. Roughness of the substrates usually causes the wettability to decrease due to the actual

surface area increasing. However, exceptions to this is when the surface textures are very rough or the liquid is inherently very well wetting. The effect that roughness on the surface has on wettability is also lessened for molten metals at high temperatures [30]. Surface porosity is also a factor. The effect of this is similar to the effect of the surface roughness [31]. Another factor is liquid penetration into the substrate. This will lead to a decrease in the measured contact angle due to a drop in the sessile volume which is illustrated in Figure 2.7 [32]. Furthermore, a lower relative density of the substrate can lead to more penetration [33]. Some other factors affecting the wettability are: Temperature, mass of the samples and impurities [32].

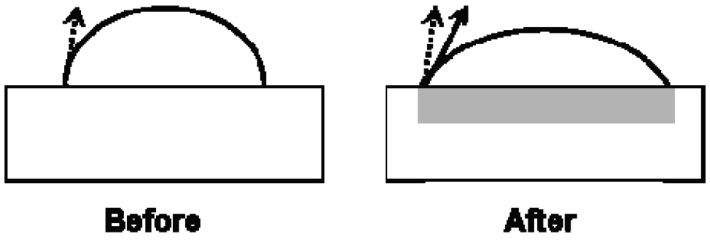

Figure 2.7: Penetration behaviour. Extracted from [32]

2.3.3 Wetting with Molten Aluminium

Investigation of the wetting properties of molten aluminium using the Sessile Drop method is difficult. The main difficulty is due to the formation of an oxide layer on the aluminium when oxygen is present. The oxidation of the aluminium is shown by the following equation:

$$4\,\mathrm{Al(l)} + 3\,\mathrm{O_2(g)} = 2\,\mathrm{Al_2O_3(s)} \tag{2.3}$$

The oxide layer has a much higher melting temperature than aluminium (660 °C for Al and 2050 °C for Al_2O_3 [34]) and can normally not be removed by heating. At normal pressure the melted aluminium will be trapped a solid shell of aluminium oxide, which makes the measurement of the contact angles impossible. The oxide layer is inevitable since the oxidation reaction will take place even at a partial pressure of oxygen as low as 10^{-49} bar at 700 °C [35]. With the current experimental apparatus it is not possible to achieve this pressure. However, at low enough pressure the oxide layer can be removed by an outgoing

flow of Al_2O gas according to the following reaction:

$$4\,Al\,(l) + Al_2O_3(s) \longrightarrow 3\,Al_2O\,(g) \tag{2.4}$$

This reaction is in equilibrium at 1000 °C and with a partial pressure of Al_2O of 4.3×10^{-5} bar [35]. Thus, at temperatures above 1000 °C the oxide layer can be removed if the pressure is lower than this partial pressure. High heating rates during operation up until this equilibrium is reached, helps reducing the thickness of the initial oxide layer. Bao et al. [35], reported total pressure in the furnace under 10^{-8} bar gave good results for measuring the contact angles between molten aluminium and solid alumina. In short, high vacuum is essential when performing wetting tests with aluminium using the Sessile Drop method.

2.3.4 Wetting of Molten Aluminium on a Carbon Substrate

There are several studies on the wetting behaviour of the Al-graphite system and the reactions that take place during the Sessile Drop wetting testing. There is a very large scattering in the experimental values recorded for the wettability of aluminium on graphite. For example, equilibrium contact angle measures at 800 °C has, dependant on the study, varied from less than 30° to more than 160° [36]. The large range of contact angles has to do with the different experimental conditions and quality of the materials.

As mentioned in section 2.3.3, the wettability of the sample on the substrate changes over time. According to Bao et al. [37], the wettability for the Al-graphite system changes with time in three stages, which are listed below. Figure 2.8 gives an illustration of the stages.

Stage 1: De-oxidation of oxide layer.

This stage is dominated by the de-oxidation of the Al_2O_3 layer around the aluminium as explained in section 2.3.3 with reaction (2.4). Stage 1 takes place before $\mathbf{t}_1$ in Figure 2.8.

Stage 2: Formation of Al_4C_3

During stage 2 aluminium reacts with the graphite and forms a layer of Al_4C_3 on the interface between the aluminium and the graphite by the following equation:

$$4\,\mathrm{Al(l)} + 3\,\mathrm{C(s)} \longrightarrow \mathrm{Al_4C_3} \tag{2.5}$$

Stage 2 takes place between $\mathbf{t}_1$ and $\mathbf{t}_2$ in Figure 2.8.

Stage 3: Stable contact angle

At the beginning of stage 3, the Al-Al_4C_3 system is formed resulting in a relative stable contact angle. Stage 3 takes place after $\mathbf{t}_2$ in Figure 2.8.

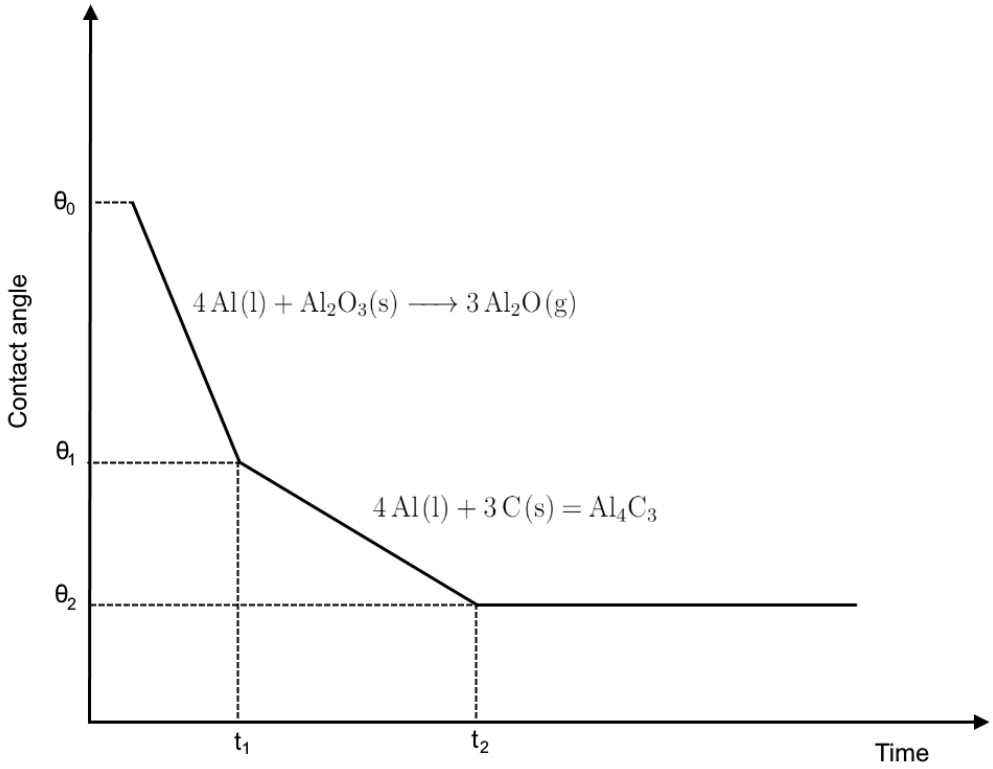

Figure 2.8: Time dependant wettability of the Al-graphite system. Based on a figure from [37]

2.3.5 Wetting of Molten Aluminium on a TiB_2 Substrate

There has been many reports on the wetting of aluminium on TiB_2. In most cases TiB_2 is reported to have excellent wetting properties towards aluminium, but there is a large scattering of contact angles ranging from 0-140° [4]. Samsonov et al. [38], did not observe any wetting of TiB_2 (theoretical density close to 95%) in the temperature range 900-1000 °C

in vacuum (value for vacuum not specified). However, contact angles of 75° an close to 30° was achieved after isothermal heating for 20min at temperatures of 1150 °C and 1250 °C, respectively. Weirauch et al. [33], tested the wetting properties of several TiB_2 substrates with different microstructures and densities. A contact angle of 0° was achieved with a sample of 99.7% theoretical density while holding a temperature of 1025 °C for 17h under a high vacuum of approximately 10^{-7} bar. The large range of contact angles has to do with the different experimental conditions and quality of the materials.

The wetting of the Al-TiB_2 system was proposed to be two stages as opposed to the three stages for the Al-graphite system [8]. Similar to the Al-graphite system, the first stage is due to de-oxidation of the oxide layer on the aluminium which was explained in section 2.3.3. In addition to this, the aluminium reacts with oxide impurities on the surface of the TiB_2 substrate. TiO_2 is reduced by aluminium according to the following equation [39]:

$$4\,Al(l) + 3\,TiO_2(s) \longrightarrow 2\,Al_2O_3(s) + 3\,Ti(l) \tag{2.6}$$

Because of this reaction, Al_2O_3 crystals nucleate at the interface between the aluminium and TiB_2. Furthermore, pure Ti is released into the molten Al, which upon cooling precipitates Al_3Ti at the Al/TiB_2 interface [8]. Aluminium does not react with TiB_2. To compare it to the Al-graphite system, after stage 1, the Al-TiB_2 system enters the final stage, resulting in a relative stable contact angle.

2.3.6 Wetting of Molten Aluminium on a C-TiB_2 Composite Substrate

There has been some attempts to test the wettability of aluminium on C-TiB_2 composite. Watson and Toguri [5], reported that the measured contact angles for the composites decreased over time, but that the contact angles would keep decreasing until the point of contact between the composite surface and the aluminium could no longer be determined, thus the equilibrium contact angles were unknown. However, the decrease in contact angle was reported to be more rapid with higher TiB_2 content in the composite. Watson and Toguri [5], also tested the wettability of C-TiB_2 composite in cryolite melts at 1000 °C and

reported contact angles of zero, after 90 minutes for composites containing 62 and 70 wt% TiB_2. How the composites were made was not specified.

Xue et al. [40], reported a steady increase in wettability of carbon-graphite-TiB_2 composites at 900 °C with increasing TiB_2 content. These composites were prepared by mixing of TiB_2, anthracite + graphite and pitch binder after witch it was heat treated at 1250 °C. It was also concluded that the time dependant contact angles had two stable stages. The first stage was associated with the layer of Al_2O_3 on the aluminium and the second stage was associated with formation of Al_4C_3.

3. Experimental

3.1 Powders and Sample Preparation

3.1.1 Powders

TiB_2 Powder

The TiB_2 powders used to make the composite samples were purchased from H.C.Starck. The powders were TiB_2-Grade F, which is a grade of TiB_2 best suited to sintering that H.C. Starck supplies. The purity and the particle size distribution the TiB_2-Grade F powder are listed in table 3.1 and 3.2 respectively. This data is obtained from H.C.Starck. The powder was chosen mainly because of the small particle size. This was to limit the possibility of cracking along the grain boundaries after sintering (explained in section 2.2.3).

Table 3.1: Chemical Characteristics of TiB_2 Grade F

Chemicals	**Grade F**
B	min. 29.5 %
C	max. 0.4 %
O	max. 2.5 %
N	max. 0.5 %
Fe	max. 0.1 %

Table 3.2: Particle size distribution of TiB_2 Grade F

Particle Size Distribution	**Grade F**
D 10 %	0.5- 1.2 µm %
D 50 %	2.5- 3.5 µm %
D 90 %	4.0- 7.0 µm %

A SEM image of this powders is shown in Figure 3.1.

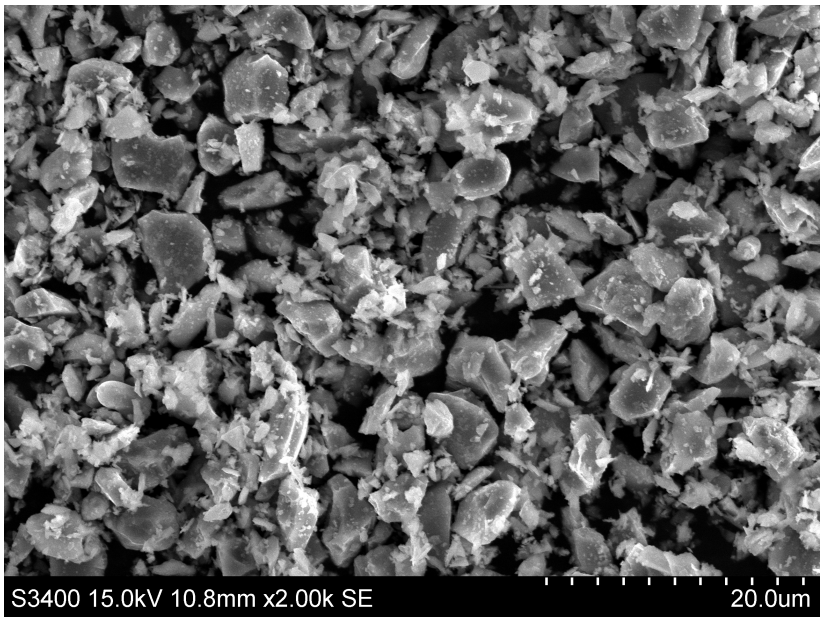

Figure 3.1: SEM image of TiB_2 powder from H.C.Starck. Taken with secondary electron detector at x2.00k magnification.

Carbon Black Powder

The carbon powder used for the composite samples were of the type Carbon black (CB), acetylene (often refered to as acetylene black) from Alfa Aesar. This powder was chosen mainly because of high purity with low ash content and small particles. A SEM image of the CB powder is shown in Figure 3.2. The mean particle size is between 25-45 nm.

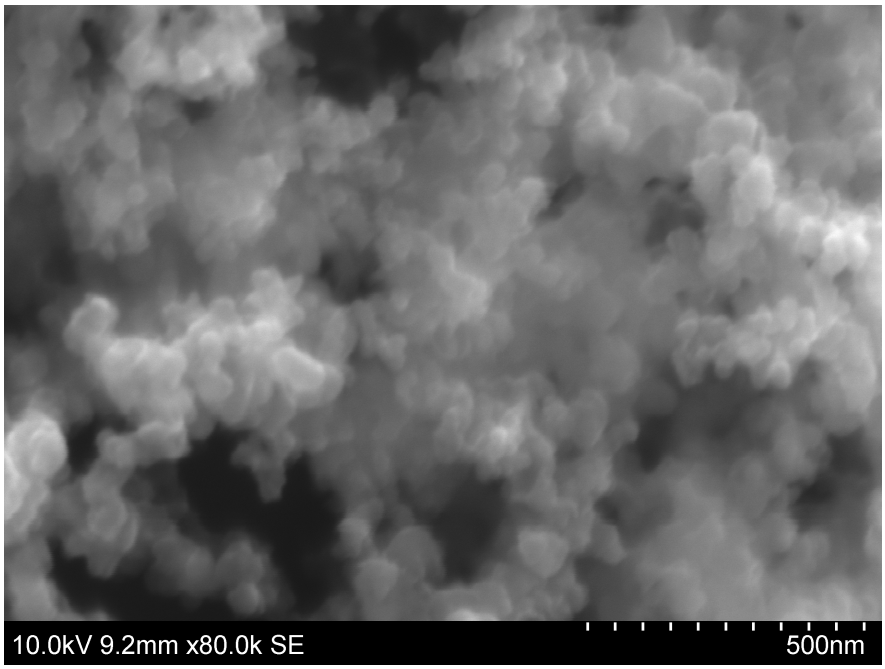

Figure 3.2: SEM image of Carbon black powder from Alfa Aesar. Taken with secondary electron detector at x80.0k magnification

3.1.2 Powder Preparation for C-TiB_2 Composites

The powders were weighed in the desired weight ratio for each sample and mixed together using a mortar and piston. The weight percentage of CB used for each sample is listed in Table 3.3. The mixed powders were then dried over night in a drying cabinet at 100 °C. After drying, the powders were sieved (250 mesh-size) to get rid of agglomerates so that a higher packing of the powders could be achieved before sintering. Lastly the mixed powders were added to dies (inner diameter 20mm) lined with graphite sheets. Pistons were added to both ends of the die with the powder, and a pressure of 50 MPa were added manually with a hydraulic press (**C-type**) to pre-pack the powders before sintering. The graphite sheets were mainly there so that the samples would not stick to the dies of pistons after sintering. The samples of pure TiB_2 were prepared the same way as the composites.

Table 3.3: Carbon Black content of the $C-TiB_2$ - composite samples.

Sample #	**Carbon Black content** [wt%]
1	15
2	25
3	35
4	45
5	55
6	65
7	75
8	85

3.2 Procedures

After the powder preparation the samples were sintered using SPS. After sintering the samples were then grinded to get rid of the graphite layer resulting from the graphite sheet lining in the die. Density of the samples were measured using Archimedes' method. Thereafter, the samples were cut into cubes for wetting testing towards molten aluminium. The wetting test was done using the Sessile Drop Method. The sample pieces that were not used for wetting, were polished to get a smooth surface so that the microstructure could be studied using Scanning Electron Microscope (SEM). After the wetting tests, the samples were cut and polished so the wetting interfaces could be studied using SEM and Energy-dispersive X-ray spectroscopy (EDS).

3.2.1 Spark Plasma Sintering

For Spark Plasma Sintering (SPS), the **SPS 825 Dr.Sinter** was used. A schematic drawing of the SPS setup is shown in Figure 3.3.

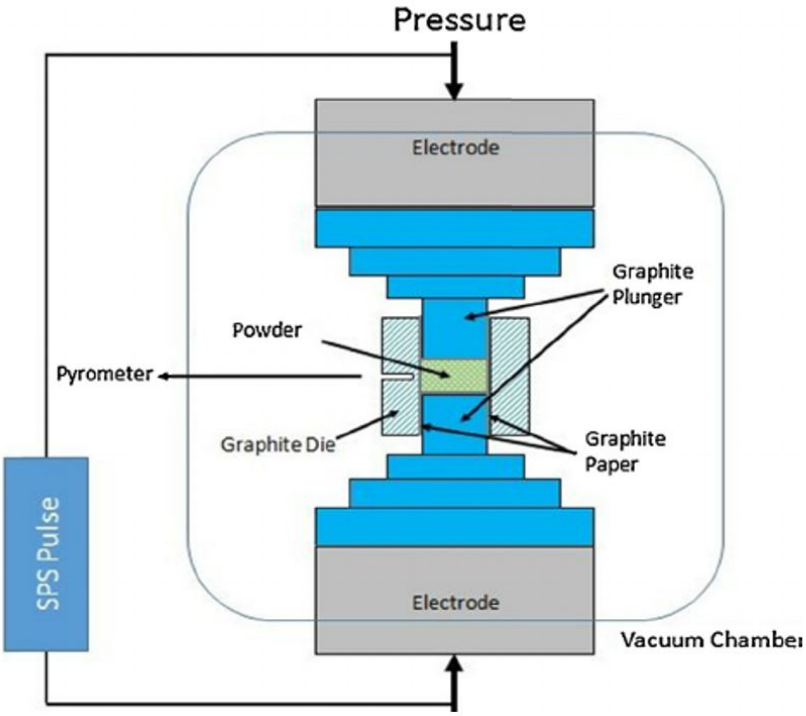

Figure 3.3: A schematic drawing of the Spark Plasma Sintering setup. Extracted from [41]

The prepared samples were loaded into the vacuum chamber in a similar manner to the illustration in Figure 3.3. Because of the high temperature required for sintering TiB_2, the die and graphite blocks (blue blocks in Figure 3.3) had to be surrounded with a layer of graphite wool and a heat shield to protect the SPS. The air was then evacuated until a pressure lower than 3×10^{-4} bar was achieved before starting the sintering process. A sintering program was made for automatic control of the temperatures and axial pressure. The program was derived in the specialization project [25] with the basis from previous investigations listed in section 2.2.3. The program used is shown in Figure 3.4.

The temperature could be measured using either a thermocouple or a pyrometer. For high temperature sintering, the pyrometer was required. The heating rates used for sintering were 150 °C/min. The pyrometer used only measured temperatures above 400 °C. Thus, the heating rate before 400 °C is not displayed in Figure 3.4, but it is actually 150 °C/min in this area as well. Because the axial pressure required exceeded 12.1 kN force, the SPS instrument had to run on a high pressure program. This meant that the instrument could go higher than 12.1 kN but not lower, which is the reason for the high initial pressure in the program.

Further explanation of the temperature profile is included in Appendix A.

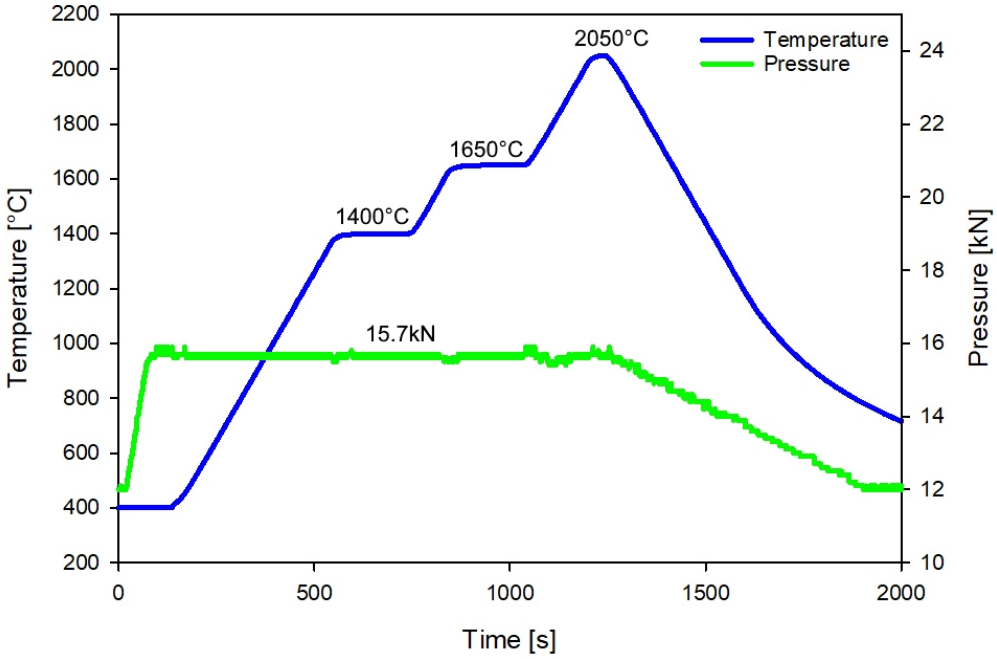

Figure 3.4: The sintering program used for SPS with temperatures in blue and the axial pressure applied in green.

3.2.2 Cutting and Surface Polishing

The samples had a layer of graphite resulting from the graphite sheets used during sintering. This was grinded of using MD-Piano 220. The samples were cut into 10x10x4 mm cubes using a high precision saw (**Stuers Accutom-5**) with a diamond blade. The dimensions of the cubes were the required for the Sessile Drop wetting testing. Cutting rate were set to 0.02 mm/min with a rotation speed of 3500 rpm. The slow speed was necessary to be able to cut through the extremely hard TiB_2 material. Parts of the sample not used for wetting, were embedded in epoxy and polished with the steps shown in Figure 3.5. The samples used for the wetting testing, were cut and polished in a similar manner after the wetting tests were completed.

Grinding

Step	PG	FG
Surface	MD-Piano 220	MD-Allegro
Abrasive	Diamond	DiaPro AllegroLargo 9
Grit/ Grain size		9 µm
Lubricant	Water	
Rotational speed [rpm]	150	150
Force[N]/ specimen	40	40
Time [min]	Until Plane	5

Polishing

Step	DP	OP
Surface	MD-Dac	MD-Chem
Abrasive	DiaPro Dac 3	OP-U NonDry
Grain size	3 µm	0.04 µm
Lubricant		
Rotational speed [rpm]	150	150
Force[N]/ specimen	30	15
Time [min]	3	1

Figure 3.5: Stuers Metalogram Method F for grinding and polishing. Extracted from [42]

3.2.3 Density Measurement

The relative density of the sintered samples were measured using Archimedes' principle. To calculate the relative density of the sintered samples, three different measurements were needed:

- Dry weight(D): This is the dry weight of the samples in air.
- Weight suspended in isopropanol(S): The samples were suspended in isopropanol in a vacuum desiccator at low pressure (<20mbar) to fill all the pores of the samples with isopropanol. The samples were then weighed while still suspended in the liquid.
- Wet weight in air(W): After measuring S, the isopropanol on the surface of the samples was quickly wiped off and the samples were weighed immediately after this before too much of the liquid in the pores could dry out.

The exterior volume (V) and the bulk density (B) of the samples were then be calculated by the following equations:

$$V = \frac{W - S}{\rho_{liq}} \tag{3.1}$$

$$B = \frac{D}{V} \tag{3.2}$$

Here, ρ_{liq} in equation (3.1) is the density of liquid used, which was isopropanol in this case. The relative density (RD) was then calculated by the following equation:

$$RD = \frac{B}{\rho_{teo}} 100\% \tag{3.3}$$

Here, ρ_{teo} is the theoretical density of the material.

3.2.4 Scanning Electron Microscopy

The microstructure of the sintered samples and the effect of the wetting tests were examined using a Scanning Electron Microscope (SEM) and a Field Emission Scanning Electron Microscope (FESEM). After polishing, the samples were coated with a thin layer of carbon by sputter coating (**Cressington 208 Carbon**) and left in a heating cabinet at 60 °C to de-gas over night. The TiB_2 powder and samples after wetting tests were investigated using a SEM (**Hitachi S-3400N**). To investigate the CB powder and to detect the different grains of TiB_2, a FESEM (**Hitachi Su-6600**) was used.

3.2.5 Sessile Drop Method

A simple sketch of the Sessile Drop method is shown in in Figure 3.6. A sample is placed on a substrate inside a graphite heating element surrounded by graphite radiation shields in a vacuum chamber.

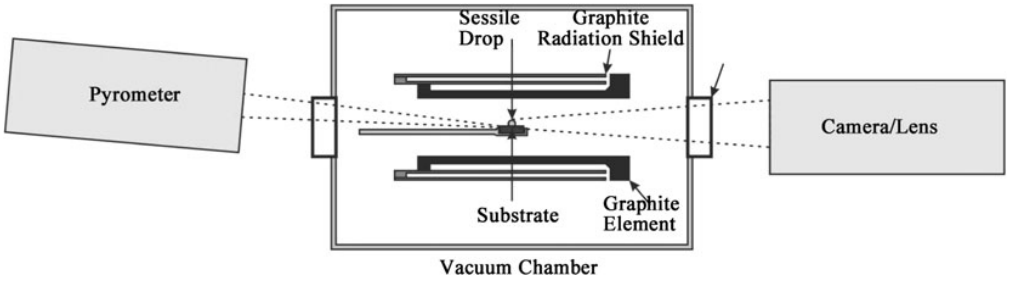

Figure 3.6: Sketch of the Sessile Drop Method setup. Extracted from [35]

In this experiment the samples were of pure aluminium and the substrates were the sintered C−TiB_2-composites. Experiments with substrates of pure TiB_2 and pure graphite (ISO-88) were also conducted (the graphite had a density of 1.9 g/cm^3). High vacuum were achieved in the vacuum chamber using a diffusion pump. Upon reaching a pressure of 9×10^{-5} bar, the heating up would start according to the heating plan presented in Figure 3.7. Rapid heating up to 900 °C was necessary to reach equilibrium of reaction (2.4) fast, so that the oxide layer on the aluminium would not form a solid shell around the melted aluminium. The alumina reduction cell runs at around 970 °C, so it would be best to get the wetting data at this temperature, but this is not practical because of the thickness of the oxide layer at this temperature. By increasing the temperature, the thickness of the oxide layer is reduced by pushing reaction (2.4) to the right, which is the reason for using the high maximum temperature of 1100 °C. The temperatures were measured using a thermocouple up to 750°C and with a pyrometer above this temperature. A camera took profile pictures of the samples during the whole process. The contact angles were then calculated using dedicated software (**FTA32 Video 2.0**).

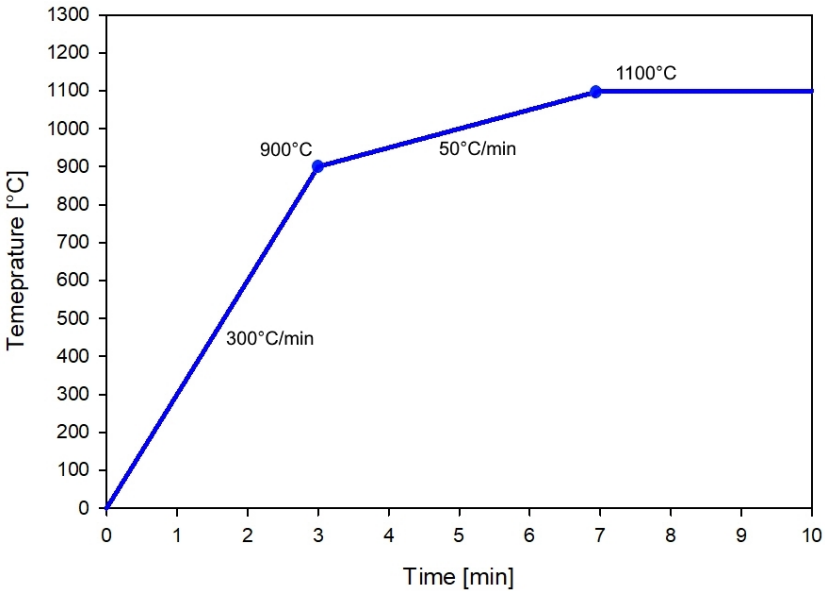

Figure 3.7: Temperature program for Sessile Drop furnace

4. Results

In this chapter, results from the experimental work are presented. The relative density and microstructure resulting from the sintering of the composites, will be presented first. Thereafter, the results from the Sessile Drop wetting tests will be presented.

4.1 Sintering of C-TiB_2

In this section, the resulting densities and microstructures from the different sinterings will be presented.

4.1.1 Density measurements

The relative density of the sintered samples were measured by Archimedes' method. The bulk densities and relative densities were calculated as explained in Section 3.2.3. The values for the bulk density, theoretical density and relative densities are listed in Table 4.1.

Table 4.1: Density measurements of the sintered samples.

Sample	**Bulk density** [g/cm^3]	**Theoretical density** [g/cm^3]	**Relative Density** [%]
Pure TiB_2	4.39	4.52	97.1
15wt% C	3.80	4.16	91.3
25wt% C	3.13	3.92	79.8
35wt% C	2.30	3.67	62.6
45wt% C	2.20	3.43	62.7
55wt% C	2.03	3.19	63.6
65wt% C	1.79	2.95	60.7
75wt% C	1.75	2.71	64.6
85wt% C	1.52	2.46	61.8

To make the comparison between the different samples easier, a graph of the relative densities was made and is shown in Figure 4.1.

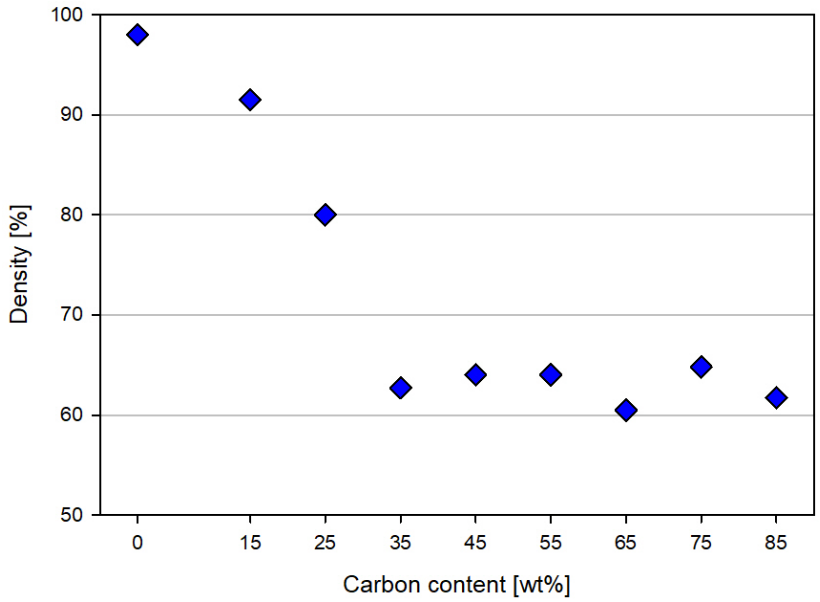

Figure 4.1: Relative density of samples measured with Archimedes' method

The relative density decreases very fast with added carbon content. The relative density for the pure TiB_2 sample is close to theoretical density. The relative density drops quick for the two next samples and stabilizes after 35wt% C is reached.

4.1.2 Microstructure

Distribution of TiB_2 and Carbon

Four SEM images are included in Figure 4.2 to show how the distribution of TiB_2 and carbon differs as the amount of carbon increases.

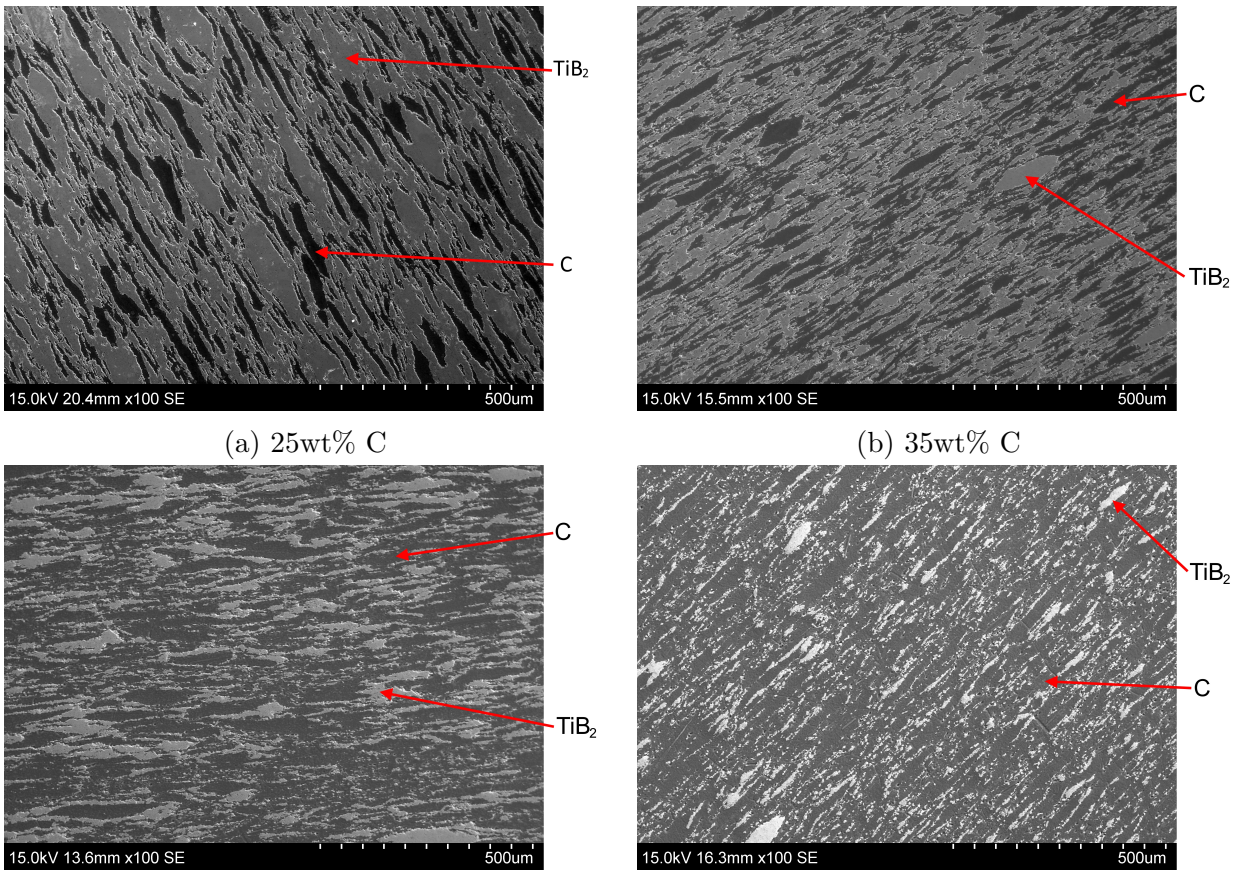

(a) 25wt% C (b) 35wt% C

(c) 45wt% C (d) 65wt% C

Figure 4.2: SEM image taken at 100x magnification with Secondary Electron detector to illustrate the different powder distributions. The images are of the crossection of the respective samples. The light gray is TiB_2 and the dark gray or black is carbon

From pure TiB_2 and up to 35wt% C, the TiB_2 is the continues phase with carbon in between. The distribution is fairly even for all four cases, but with some larger areas of either TiB_2 or carbon seemingly randomly distributed. This is more apparent the more TiB_2 is in the composite when the four images in Figure 4.2 are compared to each other. In Figure 4.2a, large areas of carbon are seen isolated by sintered TiB_2. These areas have elongated shapes. The axial pressure direction is perpendicular to these elongated shapes,

which indicates that there were agglomerates pressed together during sintering. More SEM images are included in Appendix C.

TiB_2 Grain Sizes

Three back scattered SEM images are shown in Figure 4.3 to compare the TiB_2 grain sizes. Figure 4.3a shows images for pure TiB_2 and Figures 4.3b and 4.3c shows images for the composite material with 15 wt% C.

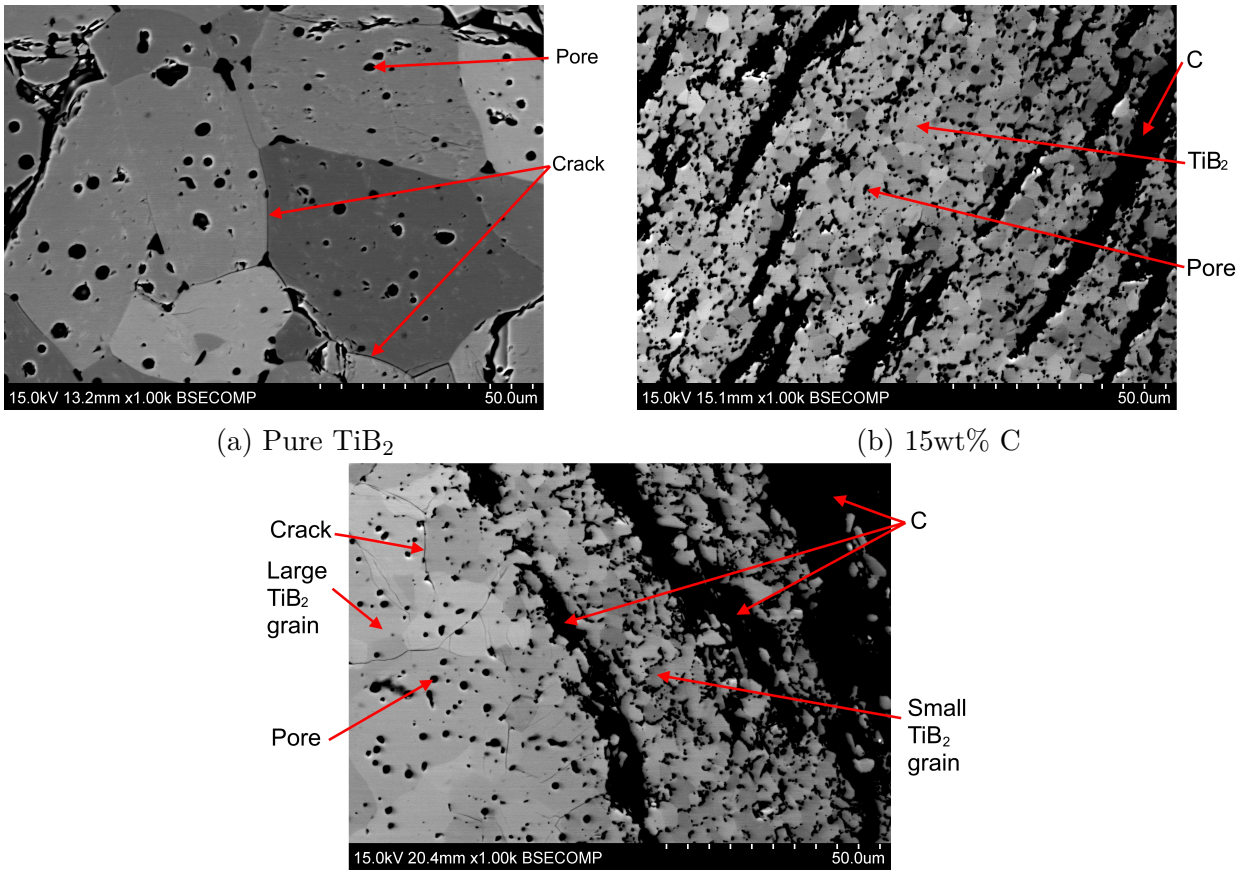

(a) Pure TiB_2

(b) 15wt% C

(c) 15wt% C

Figure 4.3: SEM image taken at 1000x magnification with Backscatter Electron detector to show the TiB_2 grain size in (a) pure TiB_2, and (b)-(c) in the composite material with 15 wt% C.

The different shades of gray indicated different orientation of the grains, which makes it easy to distinguish the different grains and measure the grain sizes. Figure 4.3a of pure TiB_2 shows very large grains. Black lines between grains indicates cracking in between these

grains. There are also several black spots in the grains, showing inter-granular pores. The perfect round shapes of some of these pores indicates that they are formed due to trapping of gas bubbles during sintering. Figure 4.3b shows much smaller grain sizes of TiB_2, however when the TiB_2 areas are larger and becomes more isolated (as shown in the left part of Figure 4.3c), the grain sizes increase. Where there are larger grains, some cracking along the grains and more inter-granular pores are evident.

4.2 Wetting

In this section the different result from the wetting will be presented. The time dependant contact angle for all the results will be presented first. After this, all the different estimated wetting stages with stage angles will be presented. Following this, comparisons of contact angles, base diameters and sessile volume will be included for some selected experiments. Finally, some SEM images of the wetting interfaces will be presented.

4.2.1 Time Dependant Contact Angle

Measuring of the contact angles started at 1050 °C after the aluminium was melted into a droplet (meaning that 1100 °C was reached 50s after the initial measurements). Only the first 1000s of each wetting test was included. This was done to make a direct comparison easier, but also because the contact angles from most of the tests lasting more than 1000s would just continue to decrease without reaching a stable contact angle. More elaboration on this in Section 4.2.2. The time dependant contact angles from all the Sessile Drop wetting experiments are shown in Figure 4.4

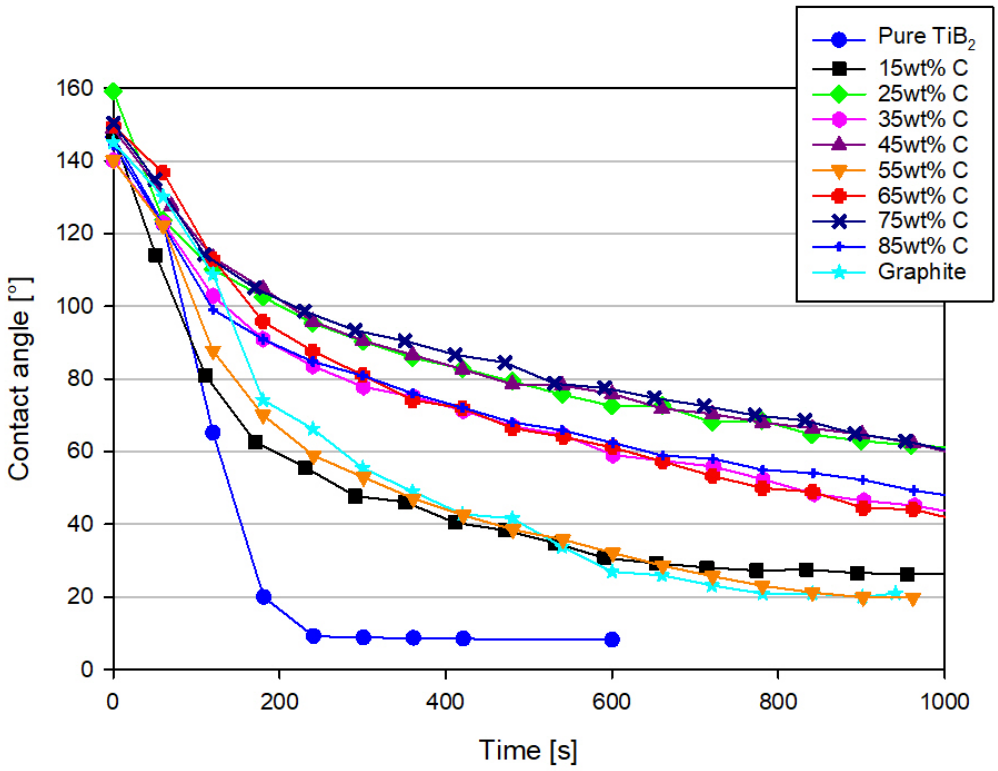

Figure 4.4: Time dependant contact angles from all the Sessile Drop wetting experiments.

The measured contact angles for the experiments, all decreased over time. The first few measurements showed a rapid decrease for all the experiments. The rate of the decrease slowed down notably for all the samples after about 200s, with the exception of the experiment with pure TiB_2, which stopped decreasing completely. The rest kept decreasing steadily for the remaining duration of the experiments with the exception of the composite with 15 wt% C and pure graphite. The contact angles for these two experiments stopped decreasing after a while. More elaboration on the individual wetting behaviour will be provided in the following two subsections.

To better illustrate the time dependant contact angles data in Figure 4.4, images from one of the experiments is shown in Figure 4.5. The images show how the wetting changes with time for the Sessile Drop experiment of the composite with 15 wt% C.

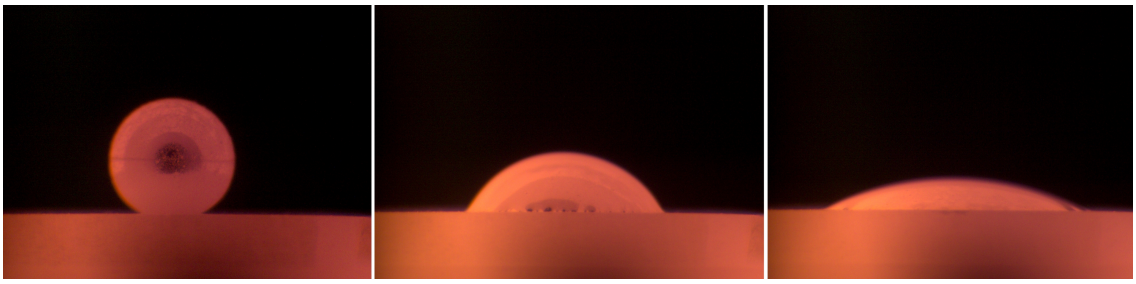

Figure 4.5: The three images shows the progression of the wetting during Sessile drop experiment of the composite with 15 wt% C. The images shows increased wetting from left to right as duration of the experiment increase. The measured contact angles of the droplets from left to right are: 147.4°, 62.6° and 28.1°

4.2.2 Wetting Stages with Estimated Stage Angles

The wetting results for the different systems can be divided into stages (see Section 2.3). The stages were determined by visual observation of the resulting time dependant contact angles. A regression line of the contact angles in each stage were then calculated. The contact angles for each stage were measured using the intersection between the vertical lines (that indicate a new stage) and the regression line of the contact angles for the following stage. The initial stage angle at the start of the experiments (stage 1) are called θ_0. The stage angles for the following stages 2 and 3 are called θ_1 and θ_2 respectively. As was mentioned in Section 4.2.1, the contact angle for most of the composites kept decreasing steadily, and no stable contact angle could be observed. For these cases, θ_s is used for the contact angle at 1000s. The wetting of pure TiB_2 follows a different time dependant wettability, and θ_1 was named θ_T instead. Estimations of the different stages and correlating stage angles for all the wetting tests are shown in Figure 4.6.

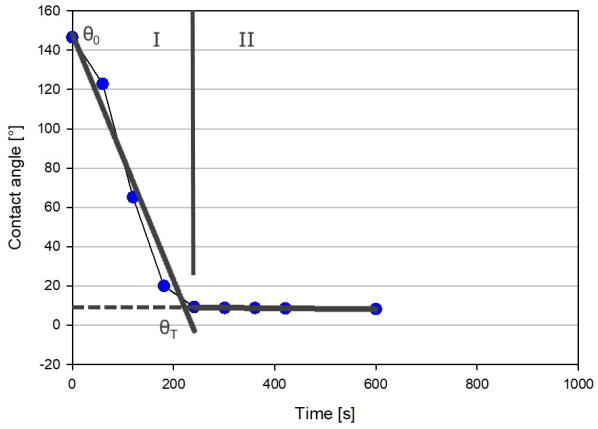

(a) Pure TiB_2

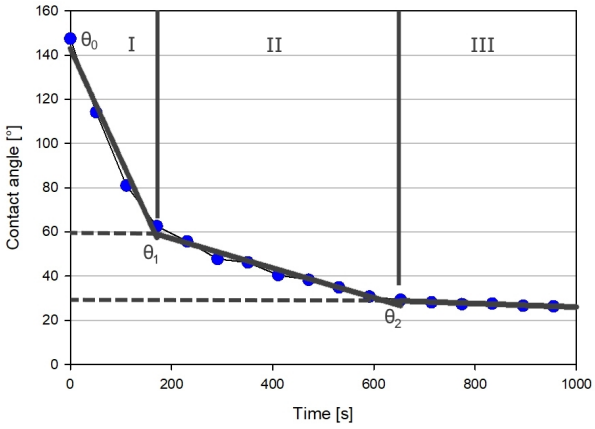

(b) 15wt% C

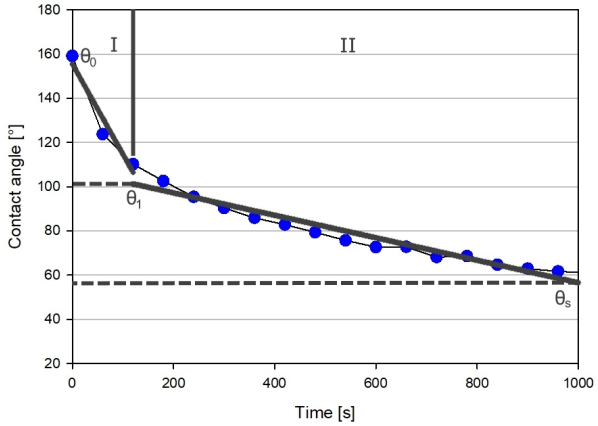

(c) 25wt% C

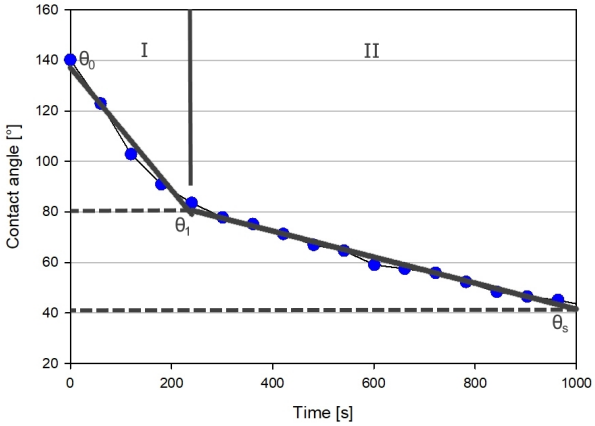

(d) 35wt% C

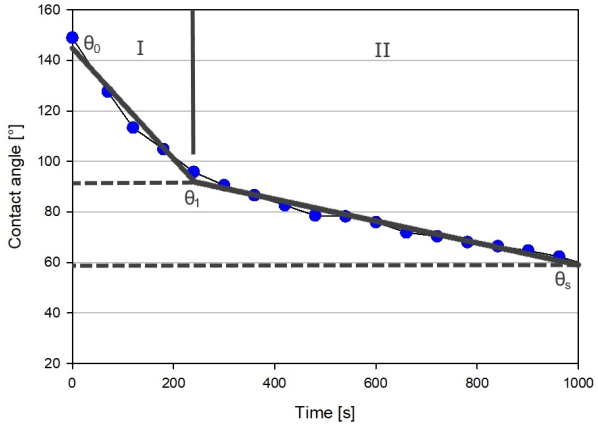

(e) 45wt% C

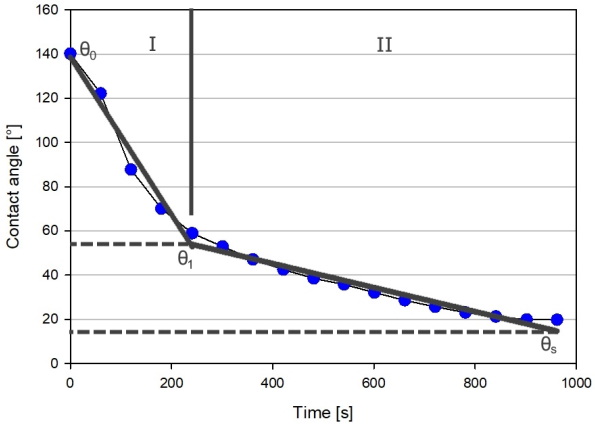

(f) 55wt% C

Figure 4.6: Stages and estimated stage angles from all the Sessile Drop wetting experiments. The vertical lines indicates a new stage. The stages are marked with roman numbers.

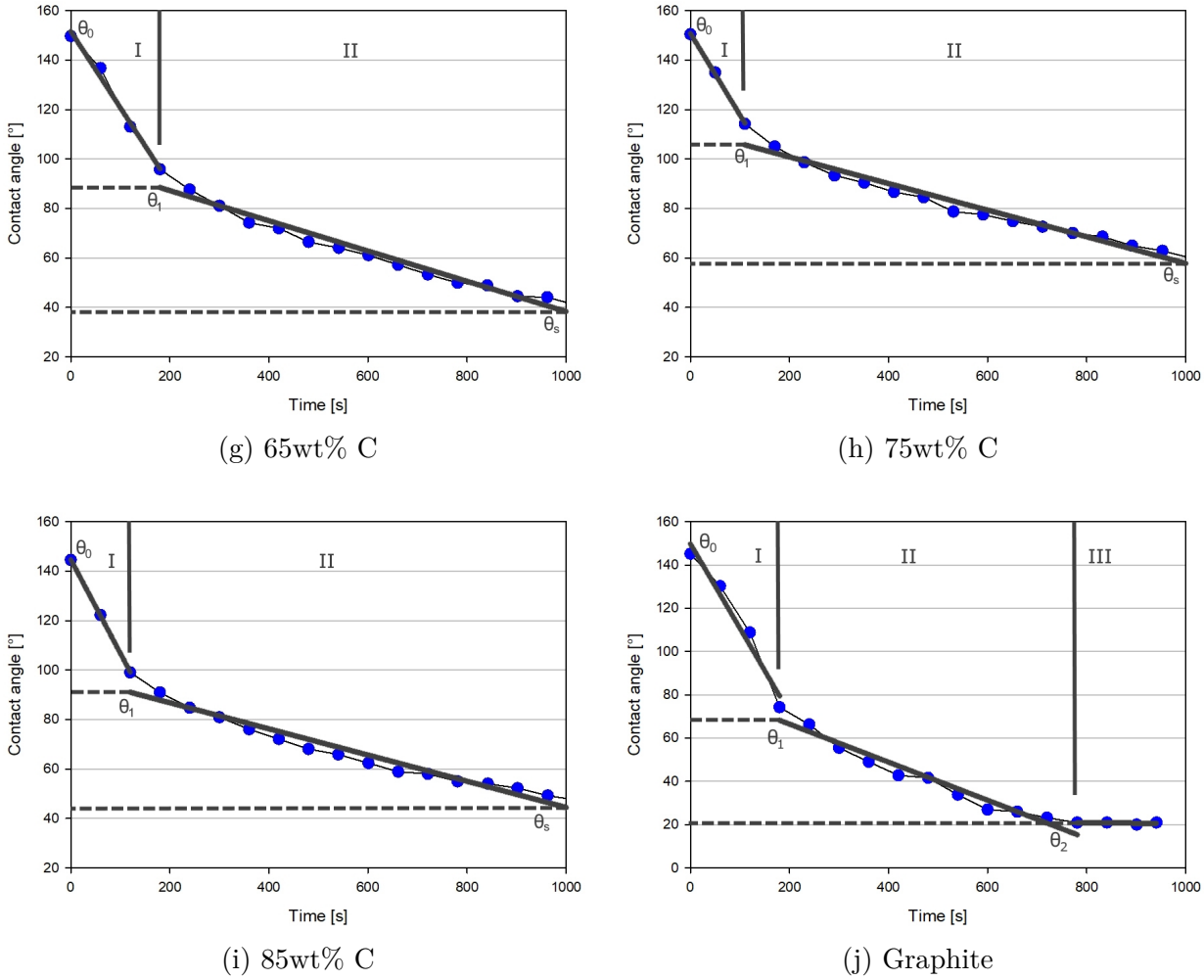

(g) 65wt% C

(h) 75wt% C

(i) 85wt% C

(j) Graphite

Figure 4.6: Stages and estimated stage angles from all the Sessile Drop wetting experiments. The vertical lines indicates a new stage. The stages are marked with roman numbers.

Figure 4.6a shows two stages for the experiment with pure TiB_2. The second stage shows a stable contact angle, therefore the stage angle calculated from this stage (θ_T) is the equilibrium contact angle for this experiment. Figures 4.6b and 4.6j shows three stages for the experiments with the composite with 15wt% C and graphite respectively. The third stage for both these experiments show stable contact angles, therefore the stage angles calculated for these stages (θ_2) are the equilibrium contact angles for these experiments. The figures for the remaining composites never reaches a stable contact angle and they are only consisting of two stages. There are no equilibrium contact angles for these experiments. All the noted angles from Figure 4.6 are listed in Table 4.2.

Table 4.2: Stage angles for the different steps during Sessile Drop wetting test

Sample	θ_0	θ_1	θ_2	θ_s	θ_T
Pure TiB_2	146.6°				9.1°
15wt% C	147.4°	53.4°	22.2°		
25wt% C	159.1°	101.3°		56.6°	
35wt% C	140.2°	80.7°		41.6°	
45wt% C	148.9°	92.0°		59.0°	
55wt% C	140.2°	53.9°		14.7°	
65wt% C	149.7°	88.5°		38.3°	
75wt% C	150.4°	105.7°		57.7°	
85wt% C	144.5°	91.1°		44.4°	
Graphite	145.2°	64.1°	11.6°		

4.2.3 Contact Angle, Base Diameter and Sessile Volume

To help understand how the contact angles have changed during the experiments, it can be useful to look at the base diameter and the sessile volume. The base diameter of a sessile drop is the measured distance of the wetting interface between the sample and the substrate. The sessile volume is the volume of the droplet. The base diameter and sessile volume is illustrated in Figure 4.7.

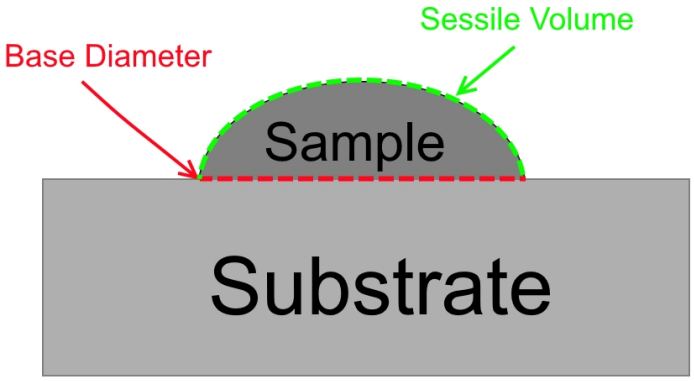

Figure 4.7: The base diameter and sessile volume of a sessile droplet. The base diameter is indicated by the red line at the wetting interface between the sample and the substrate. The sessile volume is the volume of the sample under the green line.

The change in base diameter over time shows how much the droplet (of aluminium in this case) has spread over the substrate. The calculation assumes that the droplet has spread

evenly in all directions. This is also true for the calculation of the sessile drop volume. The volume can decrease by either penetration of the aluminium into the substrate or by evaporation according to equation (2.4). To determine the cause of the change in volume, the substrates can be examined after the wetting tests to see if there is penetration of aluminium into the substrates (more on this in Section 4.2.4). A linear decrease of contact angle in combination with linear increase of the base diameter can indicate that further holding time is required in order to attain a stable contact angle. However, if the base diameter is stable and the contact angle continues to decrease, it can indicate that the stable contact angle will not be attained due to continues penetration or evaporation of the aluminium. It should be mentioned that the software used to calculate contact angle, base diameter and volume relied on manual fitting of the sessile drop shape and its base. Therefore, a small inaccuracy from one measurement to the next can be expected.

The base diameters and sessile volumes are included so that a possible trend between the different experiments can be determined. To limit the amount of data to compare, only the results of four experiments will be included in this section. In Figure 4.8 the calculated contact angles, base diameters and volumes of the sessile drops are shown for the four chosen wetting test results: Pure TiB_2, graphite and the two composites with 15wt% C and 45wt% C. All the calculations involved assumes symmetry along all axis of the droplets. Similar figures for all the samples are included in Appendix B.1.

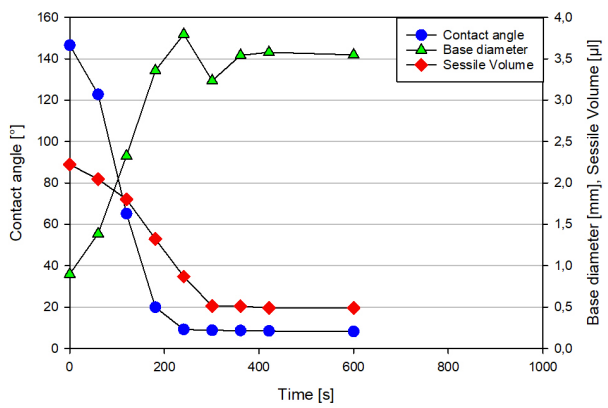

(a) Pure TiB_2

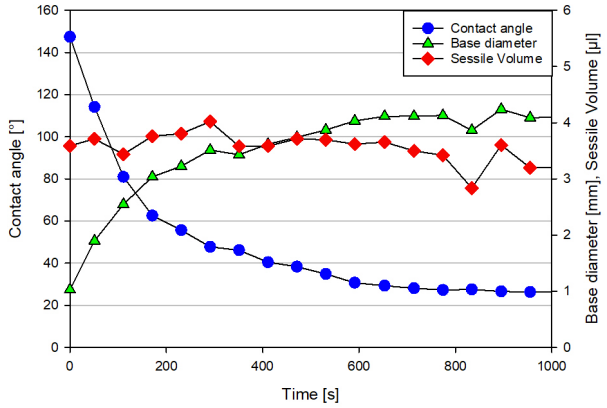

(b) 15wt% C

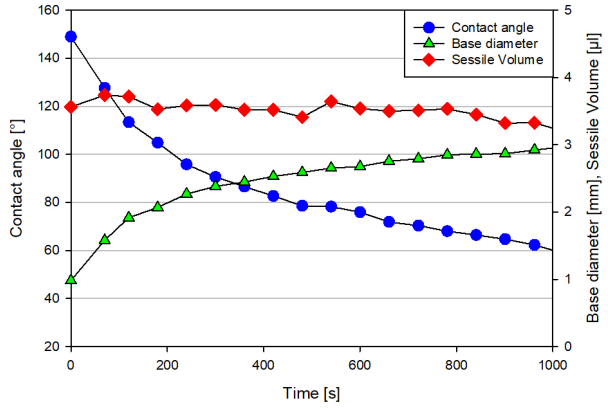

(c) 45wt% C

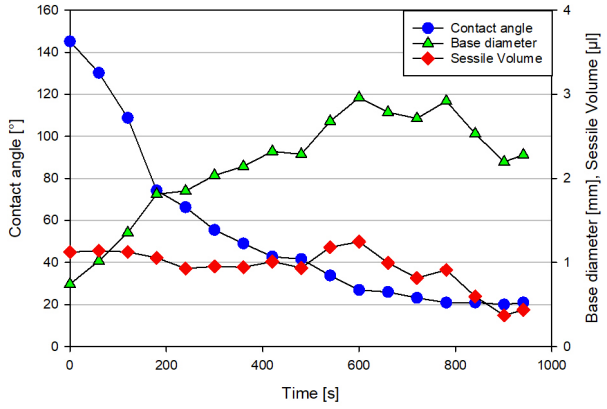

(d) Graphite

Figure 4.8: Contact angle, base diameter and sessile volume from four Sessile Drop experiments: (a) Pure TiB_2, (b) Composite with 15wt% C, Composite with 45wt% C and (d) graphite.

Figure 4.8a shows a rapid decrease of the contact angle until a stable angle is reached. There is also a very sharp decrease in the sessile volume at the start of the experiment reducing the volume of the sessile drop to around 1/4 of the original volume. This can indicate that there is much evaporation and/or penetration during this period. This much evaporation however, is very unlikely. Another possibility is that because of the high wettability of aluminium on TiB_2, the aluminium could have spread across the surface and start spreading over the sides of the substrate. This would lead to a simular volume curve as observed in the figure. However, this was not the case since aluminium was only observed on the surface of the TiB_2 material after the test. A possible explanation is that the observed base of the

sessile drop that was higher up on the sessile drop that the actual base of the droplet (due to a higher substrate or adjustments of the position of the camera). This is illustrated in Figure 4.9. The consequence of this would be that a lower percentage of the sample would be visible with decreasing contact angle, thus lowering the measured sessile volume. The base diameter in Figure 4.8a, stabilizes after the stable contact angle has been reached, indicating that equilibrium contact angle has been reached for this experiment. There is a sudden decrease in the base diameter upon reaching the stable contact angle. This can however, with high likeliness, be attributed to a miss fit of the base diameter when the contact angles were measured (manual fitting of the base diameter).

Figure 4.8b shows that the contact angle decreases rapidly for a short period, after which the rate of the decrease slows down notably before it stabilizes. The base diameter shows a steady increase which reflects the steady decrease of the contact angle. The base diameter stabilizes when the contact angle stabilizes, indicating that equilibrium contact angle has been reached. The sessile volume curve has a slight decrease overall from start to finish, which indicates low evaporation and/or aluminium penetration for the duration of the experiment.

Figure 4.8c shows rapid decrease of the contact angle for a very short period. Thereafter, the rate of the decrease slows down. The contact angle continues to decrease slowly for the rest of the experiment, indicating that no equilibrium contact angle has been reached in this experiment. The sessile volume has a steady decrease from start to finish, indicating indicates low evaporation and/or aluminium penetration for the duration of the experiment.

Figure 4.8d shows a similar contact angle behaviour to the composite with 15 wt% C seen in Figure 4.8b. The sessile volume and base diameter in the latter half of the graph, behaves irregular with unexpected increases and decreases between each measurement. The reason for this was because the fitting of the base diameter in this area became difficult because a dark smudge grew on the inside of the window where the pictures were taken from, obscuring part of the sessile drop. The contact angle could still be measured using the unobscured part of the sessile drop, but the base diameters were hard to fit correctly. From the first half of the graph, the sessile volume shows a steady decrease indicating low evaporation and/or aluminium penetration in this area.

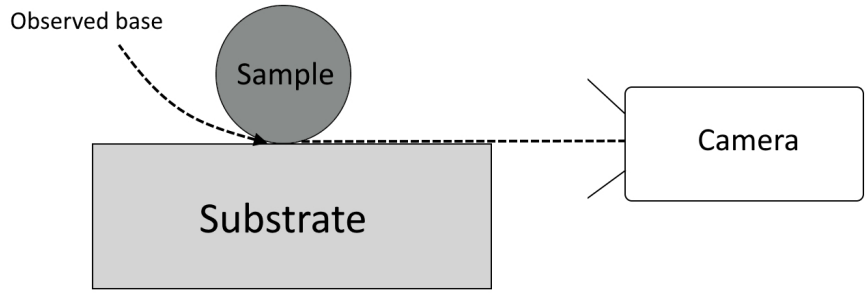

(a) Normal position of the camera

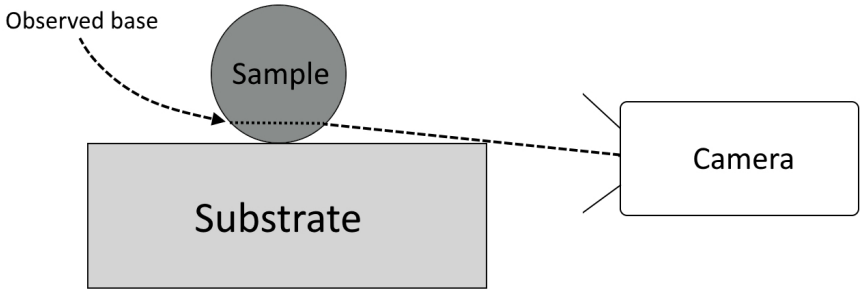

(b) Lower position of the camera

Figure 4.9: An illustration of how a different base can be observed if the substrate is higher up relative to the position of the camera during a Sessile Drop wetting experiment.

4.2.4 SEM Images of Wetting Interfaces

The interface between aluminium droplet and the composite material was examined with SEM and EDS after the wetting tests. A BSE detector was used to see the different phases at the interfaces, and point analysis was performed to determine the elemental composition of the different phases. Three of the samples were polished and examined after the wetting tests. These are from the experiments with pure TiB_2, composite with 15 wt% C and graphite. SEM images of the wetting interfaces from these three experiments are shown in Figure 4.10.

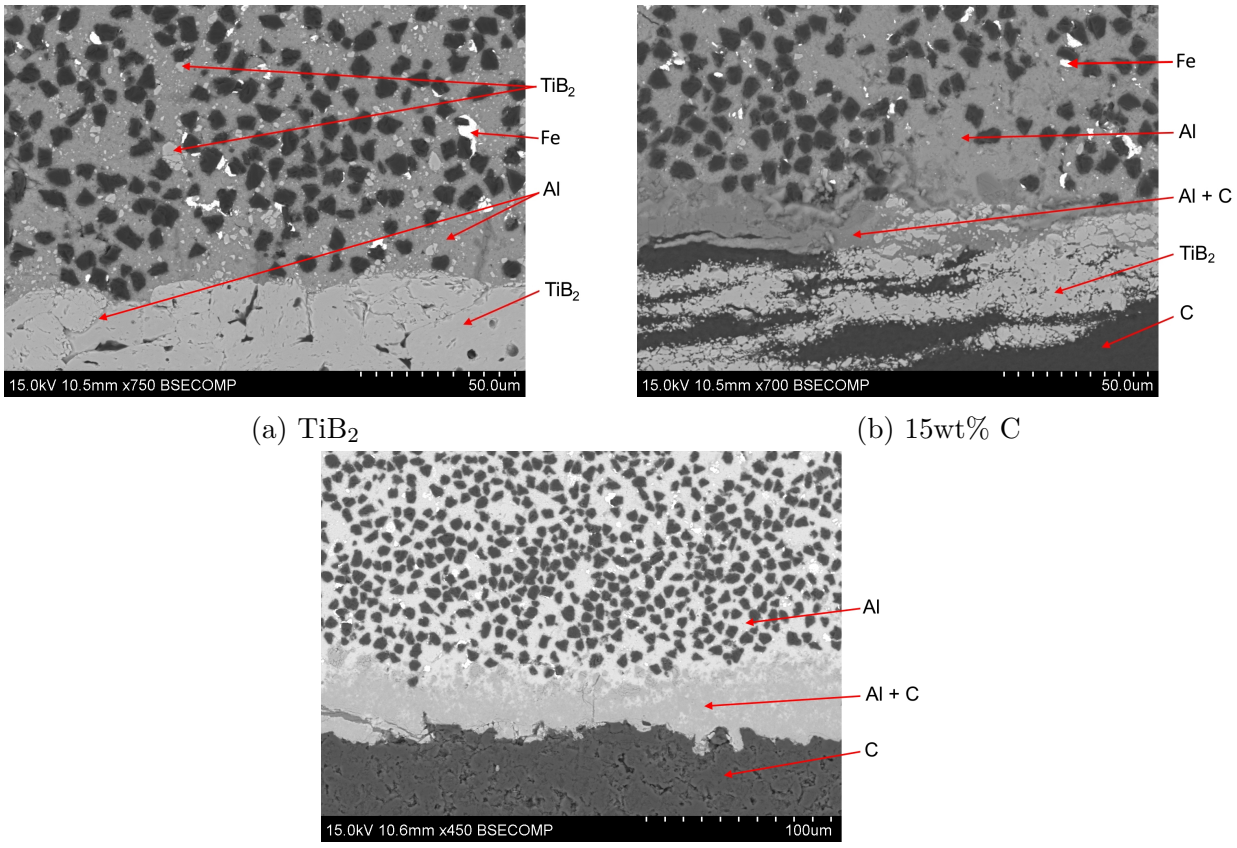

(a) TiB_2 (b) 15wt% C

(c) Graphite

Figure 4.10: SEM images of the interfaces between aluminium and three different substrates using a BSE detector. The different phases are indicated with red arrows.

In Figure 4.10a, only two layers were observed. These consisted of one layer of aluminium and one layer with TiB_2. Some particles of TiB_2 were observed in the aluminium layer. However, almost no penetration of aluminium into the TiB_2 layer were observed, with the exception of some penetrations along some of the grain boundaries indicated in the figure. Some Fe impurities were observed in the aluminum. The reason for these impurities is uncertain, but it could be impurities from the blade used when the aluminium was cut into small samples.

In Figure 4.10b, three layers were observed. These consisted of a layer of aluminium, a layer of the composite (indicated as TiB_2 and C in the lowest part in the figure) and a layer consisting of a combination of aluminium and carbon (indicated Al+C in the figure). This third layer was notably thicker between aluminium and carbon than it was between aluminium and TiB_2. Point analysis was performed of this third layer at the indicated

location in the figure and the resulting elemental composition is listed in Table 4.3. Some Fe impurities were observed in the aluminum similar to what was observed in Figure 4.10a.

Table 4.3: Point analysis at location indicated "Al+C" in Figure 4.10b.

Element	**Atomic**%
C	37.80
O	6.48
Al	55.41
Ti	0.09
Si	0.22
Total	100

In Figure 4.4, three layers were observed. These consisted of a layer of aluminum, a layer of carbon and a layer consisting of a combination of aluminium and carbon (indicated Al+C in the figure). Point analysis was performed of this third layer at the indicated location in the figure and the resulting elemental composition is listed in Table 4.4.

Table 4.4: Point analysis at location indicated "Al+C" in Figure 4.10c.

Element	**Atomic**%
C	40.67
O	1.55
Al	57.35
Si	0.43
Total	100

5. Discussion

This chapter will discuss the results presented in the previous chapter. First, the results of the sintering will be discussed including the density measurements and microstructure. Thereafter, the results from the Sessile Drop wetting experiments will be discussed.

5.1 Sintering of C-TiB_2

In this section, the densification and microstructure resulting from the sintering, will be discussed.

5.1.1 Densification of C-TiB_2

The relative densities of the sintered composites shown in Figure 4.1 varies much. The relative density of pure TiB_2 was fairly high at 97.1%, which is consistent with the relative density values listed in Table 2.2. It was expected that a small addition of carbon would increase the relative density of a sintered TiB_2 sample (see Section 2.2.3). The density of the sample would then peak at an amount of carbon resulting in total reduction of the oxide impurities in the TiB_2 powder. The amount of carbon needed to theoretically reduce all the oxide impurities (TiO_2 and B_2O_3) in the TiB_2 powder (2.5wt% oxides) has been calculated using the chemical equation (2.1) to be 1.9 wt% (assuming homogeneously distribution of both the oxide impurities and the mixed carbon). After this amount of carbon, further increase in carbon content was expected to leave residual carbon and lower the relative density of the sintered sample. The relative densities of the composites were therefore expected to decrease linearly with the amount of carbon added after 1.9 wt% carbon. This was clearly not the

case for the relative densities measured in Figure 4.1. The sintered composites had a steady decrease in the relative density until 35 wt% carbon, after which the relative density stayed about the same all the way up to 85 wt% carbon. Why this is the case is uncertain. A possible explanation is that the sintering of TiB_2 is very limited when reaching around 35 wt% carbon. If this is the case, there still will be a linear decrease due to more carbon being added, but there will in effect be an increase in density at the same time due to less poorly sintered TiB_2 in the composite.

The composites consist of both a hard material (TiB_2) and a soft material (C) and sintering of such a composite is not easily done. It often leads to high stresses in the material after sintering [43]. Optimal sintering parameters for two such materials are often very different. For a soft and hard material, this is especially true with respect to the axial pressure applied. Too high pressure can lead to stress development in the material, while too low pressure can lead to less densification [44]. Although the relative density of the most of the composite are low, the fact that the composites were sintered and not dissolving after the sintering process is impressive. Further, optimization of the sintering parameters might increase the densities of the low density composites.

5.1.2 Microstructure

The SEM images from three composites listed in Figure 4.2, show a good distribution of TiB_2 and C. These images are of the crossections of the composites. This is the reason for the elongated shapes of the larger areas consisting of either TiB_2 or C. The axial pressure direction is perpendicular to the elongated shapes, which indicates that there were agglomerates pressed together during sintering. From pure TiB_2 and up to 35 wt%C, the TiB_2 is the continues phase of the composite with carbon in between. TiB_2 wets aluminium much better than carbon, and it was therefore expected that there would be better wetting for the composites where TiB_2 was the continues phase, resulting in a noticeable drop when this was no longer the case. This will be considered when discussing the wetting results in the wetting section below.

The sintered TiB_2 sample showed very large grains (see Figure 4.3a). Due to anisotropic thermal expansion behaviour (see Section 2.2.3), this resulted in cracking along the grain

boundaries. Cracking can lower the mechanical strength of the material and it can also result in more penetration of the material during wetting. There were also many inter-granular pores observed in the material. The perfect round shapes of many of these pores indicates that they have been formed due to trapping of gas bubbles during sintering. This is likely from the formation of CO gas from carbothermic reduction of oxide impurities (equation (2.1)). Although there is no carbon in the TiB_2 powder, the sintering of the powders is taking place in a graphite environment which will react with the TiB_2 powder. This was also reported in the project report [25] (see Section 2.2.3).

Carbon content has been shown to prevent exaggerated grain growth during sintering (Section 2.2.3). This is apparent when studying Figures 4.3b and 4.3c. The grains of TiB_2 are much smaller in the composites. However, when the TiB_2 is isolated from the carbon (left part of Figure 4.3c),larger grains are observed. There are much empty space between the smaller grains, which indicates less sintering of the TiB_2 in this area. This observation agrees with the explanation given for the stable but low density of the composites given in the above section.

5.2 Wetting

In this section the wetting results will be discussed. First, a general observation and comparison of the wetting behaviour and stages will be provided. Following this, the wetting results from four individual experiments will be discussed in more detail.

5.2.1 Wetting Behaviour

It is difficult to see any apparent connection between the estimated stage angles and the carbon content. There are several ways the wetting behaviours can be compared to each other. Most ideal is to compare the equilibrium contact angles from the different experiments. Only three equilibrium contact angles were observed. These were from the experiments with pure TiB_2, composite with 15 wt% C and graphite, with equilibrium contact angles of 9.1°, 22.2° and 11.6° respectively. These equilibrium contact angles were expected to increase with increasing amount of carbon (see Sections 2.3.4 - 2.3.6). Thus, the equilibrium contact angle

of graphite was expected to be higher than for the composite with 15 wt% C, which was not the case.

Another way to compare the wetting behaviour, is to compare all the stage angles at different stages with each other. By comparing stage angles from stage 2, Xue et al. [40] reported a steady increase of the angles as carbon content increased. However, by comparing all the initial stage angles together, all stage 1 angles together and all stage 2 angles together, no apparent trend was observed from the results in this work. Watson and Toguri [5] reported that the rate of decrease of the time dependant contact angle slowed down with higher carbon content. The rate at which the time dependant contact angle decreases in this work, showed no apparent trend.

5.2.2 Wetting Results from Individual Experiments

In this subsection the experiments with pure TiB_2, composites with 15 wt% C and 45 wt% C and graphite will be discussed in more detail. This is done to try to understand the wetting behaviour better and to compare the results to the findings from literature. The four results presented in this subsection includes the three experiments where a stable contact angle stage were observed and one of the composites were no stable contact angle was observed.

Pure TiB_2

The behaviour of the wetting results from the wetting experiment of aluminium on pure TiB_2 could be divided into two stages. The two stages were similar to the de-oxidation and stable contact angle stages reported in literature for similar experiments in Section 2.3.5. Achieving a stable contact angle stage indicated that an equilibrium contact angle had been reached. This probability was further strengthened by the observations on the behaviour of the stabilized base diameter in this stable stage. The low estimated equilibrium contact angle (θ_T) of 9.1°, is in agreement with the literature findings that TiB_2 has excellent wettability towards aluminium. Little aluminium penetration was expected because of the high relative density at 97.1% of the sintered TiB_2 (see Section 2.3.2). Although, the observations of the decrease in sessile volume indicated that there could be penetration. However, almost no penetration of aluminum into the substrate was observed on inspection of the wetting

interface. Oxide impurities on the TiB_2 surface were expected to react with the aluminium according to equation (2.6) and form Al_2O_3 at the interface and Ti in the aluminium. No Al_2O_3 were observed at the interface, nor were there any sign of Ti in the aluminium. This does not conclude that the reaction didn't take place, only that the amounts were very small and difficult to notice. The effect this has on the wetting properties is therefore assumed to be negligible in this wetting experiment. The possible effect the observed Fe impurities had on the results is uncertain.

Composite with 15wt% C

The wetting behaviour from the experiment of the composite with 15 wt% C, could be divided into three stages. The three stages were similar to the three stages described for the Al-graphite system including a de-oxidation stage, a stage with formation of Al_4C_3 and a final stage with stable contact angles (see Section 2.3.4). This is in contrast to what Xue et al. [40] reported for the wetting behaviour of C-TiB_2 composites where only two stages were reported, with no final stable stage. Watson and Toguri [5], did not divide the wetting behaviour into stages, but no stable contact angle were reported for the C-TiB_2 composites. The resulting stable contact angle stage from this experiment, indicates that an equilibrium contact angle (θ_2) was reached, which was estimated to be 22.2°. The observations of the stabilizing base diameters in the stable contact angle stage, also indicates that equilibrium contact angle has been reached.

At the wetting interface, three layers were observed. The third layer (formation of a new layer between sample and substrate) was expected from the reported Al_4C_3 layers observed for both wetting tests on C and on C-TiB_2 composites (see Sections 2.3.4 and 2.3.6). The formation of Al_4C_3 was reported to takes place during stage 2 of the wetting by reaction (2.5). The atomic ratio of C and Al measured with EDS at this layer, further indicates that this could be a layer of Al_4C_3. No formations of Al_2O_3 or Ti, due to reacting (2.6), were observed at the wetting interface. Little aluminium penetration was observed at the wetting interface which was consistent with the observation of the almost flat sessile volume curve. The possible effect the observed Fe impurities had on the results is uncertain.

Composite with 45wt% C

The wetting behaviour from the experiment with 45 wt% C, could be divided into two stages. The two stages were similar to the two first stages of the Al-graphite system, described in Section 2.3.4 with a de-oxidation stage and the stage with formation of Al_4C_3. No stable stage was observed in this experiment, thus no equilibrium contact angle could be estimated. This is consistent with previous wetting tests of C-TiB_2 composites reported in literature (see Section 2.3.6). Because of the low relative density of the composite, aluminium penetration into the substrate was expected (see Section 2.3.2). The wetting interface was not investigated with SEM, so possible penetration could not be observed. However, the low decrease of the observed volume curve for this experiment, indicated very low aluminium penetration.

Graphite

The wetting behaviour from the experiment with graphite, could be divided into three stages. This is consistent with the stages reported for the Al-graphite system with a de-oxidation stage, a stage with formation of Al_4C_3 and a stable stage (see Section 2.3.4). The resulting stable contact angle stage from this experiment, indicates that an equilibrium contact angle (θ_2) had been reached, which was estimated to be 11.6°. This equilibrium contact angle is low compared to what was expected from the literature findings (see Section 2.3.4). The measurements of the base diameter in the stable contact angle stage was compromised, and can not be used to for further indication that equilibrium contact angle was reached.

At the wetting interface, three layers were observed. Similar to what was discussed for the 15 wt% C composite, a third layer was expected from the reported Al_4C_3 layers observed for wetting tests on graphite (see Section 2.3.4). The atomic ratio of C and Al measured with EDS at this layer, also indicates that this could be a layer of Al_4C_3. Aluminium penetration was difficult to determine from the interface. The sessile volume curve showed very little decrease in the first half of the figure, indicating little penetration. However, the latter half of the curve was compromised, so the total volume reduction of the sessile volume could not be measured, thus the volume curve can not give any good indication.

Final remarks

The discussion of the four individual results above, yielded valuable information of the individual results. However, they did not give any further indications as to a possible wetting behaviour trend with respect to the carbon content. In order to determine a trend, more experiments should be conducted.

6. Conclusion and Further Work

C-TiB_2 composites were successfully sintered with Spark Plasma Sintering up to 85 wt% C. Almost theoretical density of pure TiB_2 was obtained with 97.1% relative density. Composites with 15 wt% C and 25 wt% had relatively high relative density at 91.3% and 79.8% respectively. The relative density of composites ranging from 35 wt% C to 85 wt% C were however limited at just above 60%. The sintering parameters used, was derived from a project work to sinter pure TiB_2. Sinter parameters for C-TiB_2 composites have room for optimization.

Time dependant wetting angles have been measured for pure TiB_2 and graphite, in addition to C-TiB_2 composites ranging from 15 wt% C to 85 wt% C. Wetting stages have been fitted and contact angles for the different stages have been reported. Equilibrium wetting angles have been reached for three samples, including pure TiB_2, composite with 15 wt% C and graphite at 9.1°, 22.2° and 11.6° respectively. For the other samples, no stages with stable contact angle were reached and the equilibrium wetting angles for these samples could not be determined. Comparison of the different stage wetting angles for the samples did not affirm any apparent trends.

Suggestions to further work is focus on optimization of the sintering parameters for sintering C-TiB_2 composites to get denser samples. Furthermore, reproducing the wetting data with several samples for each composition might help discover a trend in the wetting behaviour between the different compositions. In addition, wetting data for industrial cathode samples can be measured and be compared to the sintered C-TiB_2 composites to see how it differs from the wetting measurements with graphite reported in this work. Sintering and wetting measurements for other possible TiB_2 composites is also an option.

Bibliography

[1] R Lumley. Fundamentals of aluminium metallurgy : production, processing and applications. Elsevier, 2010.

[2] International Aluminium Institute: primary aluminium production. http://www.world-aluminium.org/statistics/#data. Accessed: 10.12.2017.

[3] T.R. Beck. Hall and héroult and the discovery of aluminum electrolysis. *Electrochemical Society Interface*, 23(2):36–37, 2014. ISSN 10648208.

[4] Morten Sundheim Jensen. Hot pressing and degradation of tib2 inert cathodes. NTNU, Tronheim, Norway. PhD Dissertation, 2009.

[5] K. D. Watson and J. M. Toguri. The wettability of carbon/tib2 composite materials by aluminum in cryolite melts. *Metallurgical Transactions B*, 22(5):617–621, Oct 1991. ISSN 1543-1916. doi: 10.1007/BF02679016. URL https://doi.org/10.1007/BF02679016.

[6] Xiaoyan Ma, Changrong Li, Zhenmin Du, and Weijing Zhang. Thermodynamic assessment of the ti–b system. *Journal of Alloys and Compounds*, 370(1):149 – 158, 2004. ISSN 0925-8388. doi: https://doi.org/10.1016/j.jallcom.2003.09.017. URL http://www.sciencedirect.com/science/article/pii/S092583880300923X.

[7] Ronald G. Munro. Material properties of titanium diboride. *Journal of Research of the National Institute of Standards and Technology*, 105(5), September 2000. ISSN 1044-677X.

[8] L. Xi, I. Kaban, R. Nowak, B. Korpała, G. Bruzda, N. Sobczak, N. Mattern, and J. Eckert. High-temperature wetting and interfacial interaction between liquid al and tib2 ce-

ramic. *Journal of Materials Science*, 50(7):2682–2690, Apr 2015. ISSN 1573-4803. doi: 10.1007/s10853-015-8814-6. URL https://doi.org/10.1007/s10853-015-8814-6.

[9] David W Richerson. Modern ceramic engineering : properties, processing, and use in design, 2006.

[10] C E J Dancer. Flash sintering of ceramic materials. *Materials Research Express*, 3(10), October 2016. ISSN 2053-1591.

[11] Marta Suárez, J.L Menendez, Ramón Torrecillas, and Adolfo Fernández. Challenges and opportunities for spark plasma sintering: A key technology for a new generation of materials. In Burcu Ertug, editor, *Sintering Applications*, chapter 13. InTech, Rijeka, 2013. doi: 10.5772/53706. URL https://doi.org/10.5772/53706.

[12] Dustin M. Hulbert, Andre Anders, Dina V. Dudina, Joakim Andersson, Dongtao Jiang, Cosan Unuvar, Umberto Anselmi-Tamburini, Enrique J. Lavernia, and Amiya K. Mukherjee. The absence of plasma in"spark plasma sintering". *Journal of Applied Physics*, 104, 2008. ISSN 0021-8979.

[13] U. Anselmi-Tamburini, J.E. Garay, Z.A. Munir, A. Tacca, F. Maglia, G. Chiodelli, and G. Spinolo. Spark plasma sintering and characterization of bulk nanostructured fully stabilized zirconia: Part ii. characterization studies. *Journal of Materials Research*, 19 (11):3263–3269, 2004. doi: 10.1557/JMR.2004.0424.

[14] Zhaohui Zhang, Fuchi Wang, Lin Wang, Shukui Li, and S. Osamu. Sintering mechanism of large-scale ultrafine-grained copper prepared by sps method. *Materials Letters*, 62(24): 3987 – 3990, 2008. ISSN 0167-577X. doi: https://doi.org/10.1016/j.matlet.2008.05.036. URL http://www.sciencedirect.com/science/article/pii/S0167577X08005028.

[15] Zhao-Hui Zhang, Zhen-Feng Liu, Ji-Fang Lu, Xiang-Bo Shen, Fu-Chi Wang, and Yan-Dong Wang. The sintering mechanism in spark plasma sintering – proof of the occurrence of spark discharge. *Scripta Materialia*, 81:56 – 59, 2014. ISSN 1359-6462. doi: https://doi.org/10.1016/j.scriptamat.2014.03.011. URL http://www.sciencedirect.com/science/article/pii/S1359646214001080.

[16] Dustin M. Hulbert, André Anders, Joakim Andersson, Enrique J. Lavernia, and Amiya K. Mukherjee. A discussion on the absence of plasma in spark plasma sintering. *Scripta Materialia*, 60(10):835 – 838, 2009. ISSN 1359-6462. doi: https://doi.org/10.1016/j.scriptamat.2008.12.059. URL `http://www.sciencedirect.com/science/article/pii/S1359646208008907`.

[17] Z.H. Zhang, X.B. Shen, F.C. Wang, S.K. Lee, and L. Wang. Densification behavior and mechanical properties of the spark plasma sintered monolithic tib 2 ceramics. *Materials Science Engineering A*, 527(21):5947–5951, 2010. ISSN 0921-5093.

[18] Matt K. Ferber, Paul F. Becher, and Cabell B. Finch. Effect of microstructure on the properties of tib2 ceramics. *Journal of the American Ceramic Society*, 66(1):C–2–C–3, 1983. ISSN 1551-2916. doi: 10.1111/j.1151-2916.1983.tb09974.x. URL `http://dx.doi.org/10.1111/j.1151-2916.1983.tb09974.x`.

[19] Weimin Wang, Zhengyi Fu, Hao Wang, and Runzhang Yuan. Influence of hot pressing sintering temperature and time on microstructure and mechanical properties of tib2 ceramics. *Journal of the European Ceramic Society*, 22(7):1045 – 1049, 2002. ISSN 0955-2219. doi: https://doi.org/10.1016/S0955-2219(01)00424-1. URL `http://www.sciencedirect.com/science/article/pii/S0955221901004241`.

[20] R. Königshofer, S. Fürnsinn, P. Steinkellner, W. Lengauer, R. Haas, K. Rabitsch, and M. Scheerer. Solid-state properties of hot-pressed tib2 ceramics. *International Journal of Refractory Metals and Hard Materials*, 23(4):350 – 357, 2005. ISSN 0263-4368. doi: https://doi.org/10.1016/j.ijrmhm.2005.05.006. URL `http://www.sciencedirect.com/science/article/pii/S0263436805000764`. Science of hard materials-8. Part I. Selected papers from the 8th International Conference on the Science of Hard Materials.

[21] Sulima Iwona, L Jaworska, Paweł Pałka, Paweł Hyjek, and Pawel Kurtyka. Influence of sintering temperature and crb2 addition on properties of titanium diboride produced by spark plasma sintering. 16:30–36, 01 2016.

[22] Morten Sundheim Jensen, Mari-Ann Einarsrud, and Tor Grande. The effect of surface oxides during hot pressing of tib2. *Journal of the American Ceramic Society*, 92(3):

623–630, 2009. ISSN 1551-2916. doi: 10.1111/j.1551-2916.2009.02923.x. URL http://dx.doi.org/10.1111/j.1551-2916.2009.02923.x.

[23] Jia Lin, Yihang Yang, Houan Zhang, Zhuxing Wu, and Yu Huang. Effect of sintering temperature on the mechanical properties and microstructure of carbon nanotubes toughened tib2 ceramics densified by spark plasma sintering. *Materials Letters*, 166 (Supplement C):280 – 283, 2016. ISSN 0167-577X. doi: https://doi.org/10.1016/j.matlet.2015.12.122. URL http://www.sciencedirect.com/science/article/pii/S0167577X1531082X.

[24] Sunggi Baik and Paul F. Becher. Effect of oxygen contamination on densification of tib 2. *Journal of the American Ceramic Society*, 70(8):527–530, 1987. ISSN 0002-7820.

[25] Audun Håberg. C-TiB_2 composite inert cathode material by spark plasma sintering - spark plasma sintering of TiB_2. NTNU, Trondheim, Norway. Specialization Project, 2017.

[26] Ahmed Thabet Mohamed and Khaled Ebnalwaled. Improvement of surface energy properties of pvc nanocomposites for enhancing electrical applications. 110, 06 2017.

[27] Vilde Stubberud Haslund. Wetting testing of wettable cathodes for aluminium production. NTNU, Trondheim, Norway. Master Thesis., 2017. URL http://hdl.handle.net/11250/2452628.

[28] Vincent Makala. Substrate Wetting: Wetting agents selection. https://coatings.specialchem.com/selection-guide/leveling-agents-for-coatings#surface%20tension%20&%20contact%20angle. Accessed: 30.06.2018.

[29] B. Schwarz, C. Eisenmenger-Sittner, and H. Steiner. Construction of a high-temperature sessile drop device. *Vacuum*, 82(2):186 – 188, 2007. ISSN 0042-207X. doi: https://doi.org/10.1016/j.vacuum.2007.07.033. URL http://www.sciencedirect.com/science/article/pii/S0042207X07002461. Proceedings of the 11th Joint Vacuum Conference (JVC-11).

[30] S. J. Hitchcock, N. T. Carroll, and M. G. Nicholas. Some effects of substrate roughness on wettability. *Journal of Materials Science*, 16(3):714–732, Mar 1981. ISSN 1573-4803. doi: 10.1007/BF02402789. URL `https://doi.org/10.1007/BF02402789`.

[31] A. B. D. Cassie and S. Baxter. Wettability of porous surfaces. *Trans. Faraday Soc.*, 40:546–551, 1944. doi: 10.1039/TF9444000546. URL `http://dx.doi.org/10.1039/TF9444000546`.

[32] Sarina Bao. Filtration of aluminium-experiments, wetting and modelling, 2011.

[33] D. A. Weirauch, W. J. Krafick, G. Ackart, and P. D. Ownby. The wettability of titanium diboride by molten aluminum drops. *Journal of Materials Science*, 40(9):2301–2306, May 2005. ISSN 1573-4803. doi: 10.1007/s10853-005-1949-0. URL `https://doi.org/10.1007/s10853-005-1949-0`.

[34] Robert A Lewis, Michael D. Larrañaga, Richard J. Lewis, and Gessner G Hawley. *Hawley's Condensed Chemical Dictionary*. John Wiley Sons Inc, sixteenth edition edition, 2016. ISBN 1118135156.

[35] Sarina Bao, Kai Tang, Anne Kvithyld, Merete Tangstad, and Thorvald Engh. Wettability of aluminum on alumina. *Metallurgical and Materials Transactions B*, 42(6): 1358–1366, December 2011. ISSN 1073-5615.

[36] K. Landry, S. Kalogeropoulou, and N. Eustathopoulos. Wettability of carbon by aluminum and aluminum alloys. *Materials Science and Engineering: A*, 254(1):99 – 111, 1998. ISSN 0921-5093. doi: https://doi.org/10.1016/S0921-5093(98)00759-X. URL `http://www.sciencedirect.com/science/article/pii/S092150939800759X`.

[37] S. Bao, A. Kvithyld, T.A. Engh, and M. Tangstad. Wettability of aluminium with sic and graphite in aluminium filtration. pages 775–782, 2011. ISBN 9781118029350.

[38] G. V. Samsonov, A. D. Panasyuk, and M. S. Borovikova. Contact reaction between refractory compounds and liquid metals. *Soviet Powder Metallurgy and Metal Ceramics*, 12(5):403–407, May 1973. ISSN 1573-9066. doi: 10.1007/BF00791269. URL `https://doi.org/10.1007/BF00791269`.

[39] S. Avraham and W. D. Kaplan. Reactive wetting of rutile by liquid aluminium. *Journal of Materials Science*, 40(5):1093–1100, Mar 2005. ISSN 1573-4803. doi: 10.1007/s10853-005-6922-4. URL https://doi.org/10.1007/s10853-005-6922-4.

[40] J. Xue, X. Chen, Y. Gao, and J. Zhu. Wettability of liquid aluminum on carbon/graphite/tib 2 composite cathode materials. pages 383–386, 2010. ISBN 9780873397476.

[41] Dmitry O. Moskovskikh, Ya-Cheng Lin, Alexander S. Rogachev, Paul J. McGinn, and Alexander S. Mukasyan. Spark plasma sintering of sic powders produced by different combustion synthesis routes. *Journal of the European Ceramic Society*, 35(2):477 – 486, 2015. ISSN 0955-2219. doi: https://doi.org/10.1016/j.jeurceramsoc.2014.09.014. URL http://www.sciencedirect.com/science/article/pii/S0955221914004907.

[42] Stuers: Grinding and polishing. https://www.struers.com/en-GB/Knowledge/Grinding-and-polishing#grinding-polishing-about. Accessed: 30.06.2018.

[43] Mark Tillman, Julie A. Yeomans, and Robert A. Dorey. The effect of a constraint on the sintering and stress development in alumina thick films. *Ceramics International*, 40(7, Part A):9715 – 9721, 2014. ISSN 0272-8842. doi: https://doi.org/10.1016/j.ceramint.2014.02.054. URL http://www.sciencedirect.com/science/article/pii/S0272884214002533.

[44] Randall M. German. Chapter ten - sintering with external pressure. In Randall M. German, editor, *Sintering: from Empirical Observations to Scientific Principles*, pages 305 – 354. Butterworth-Heinemann, Boston, 2014. ISBN 978-0-12-401682-8. doi: https://doi.org/10.1016/B978-0-12-401682-8.00010-0. URL http://www.sciencedirect.com/science/article/pii/B9780124016828000100.

A. Sintering Program

In this section the reasoning behind the temperature profile of the sintering program is explained.

Two examples of raw sintering data from two SPS sinterings are listed in Figures A.1 and A.2. The four parameters presented in the SPS data figures are:

- **Temperature:** The change in temperature.
- **Pressure:** The change in applied axial pressure.
- **Displacement:** Relative change of position from the original position of the electrodes in the axial pressure direction (see Figure 3.3). The positive direction is inwards, towards the powder, meaning that positive displacement is presented when the sample gets more compact.
- **Vacuum:** The change in air pressure within the vacuum chamber.

The two figures shows different temperature profiles. Figure A.1 shows an example of a sintering of pure TiB_2 using an old sintering program used in the specialization project [25]. This shows steady heating up to the maximum temperature. Figure A.2 shows an example of one of the composites with the sintering program used for all composites. This program shows holding times of the temperature at both 1400 °C and 1650 °C. The samples using the old program had very high porosity. Most of these pores had a perfect round shape, indicating that they were a result from trapping of gas bubbles during sintering. The formation of gas during the sintering was in the specialization project determined to be due to the carbothermic reduction of oxide impurities in the TiB_2 powder by equation (2.1). This

was from the increase in the vacuum curve, starting at around 1300 °C in Figure A.1. The vacuum pump was continuously pumping during the process, which is the reason for the decrease in pressure after the increase. The reason for the holding times in the new sintering program was to try to release gas before sintering would take place and thereby reducing the porosity of the samples. The sintering for both examples takes place at the sharp increase of the displacement curves close to maximum temperature. The sharp increase indicates densification of the sample. By using the new program, more gas was released during the process as shown by the larger area under the vacuum curve in Figure A.2. However, by comparing two samples of pure TiB_2 using the different program, no noticeable difference in porosity was detected. Despite no noticeable difference in porosity, the program used for the sintering in Figure A.2 was used for all the sintering of the samples presented in this report.

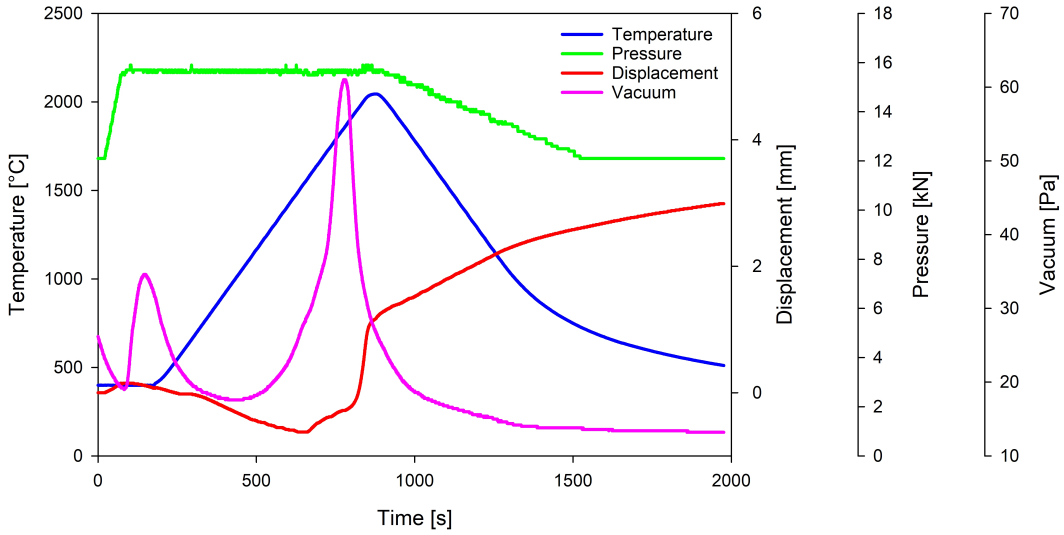

Figure A.1: Change in sintering parameters as a function of time. The data is from one of the previous sinterings of pure TiB_2 performed in the specialization project [25].

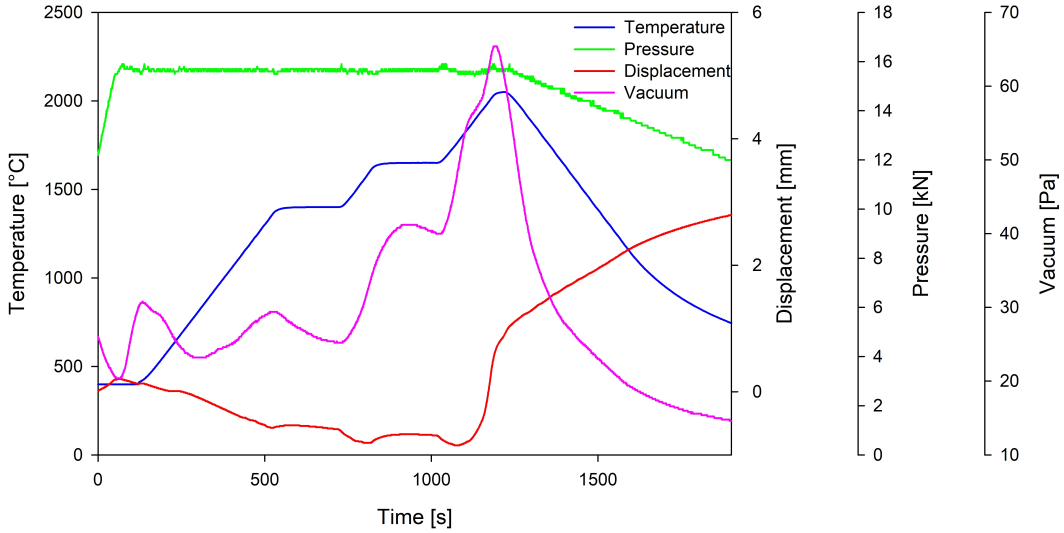

Figure A.2: Change in sintering parameters as a function of time. The data is from the sintering of the composition of TiB_2 with 25wt% C.

B. Wetting Data

B.1 Contact angle, Base Diameter and Sessile Volume comparison

All calculated contact angles, base diameter and volumes comparisons from the Sessile Drop experiments are shown in Figure B.1

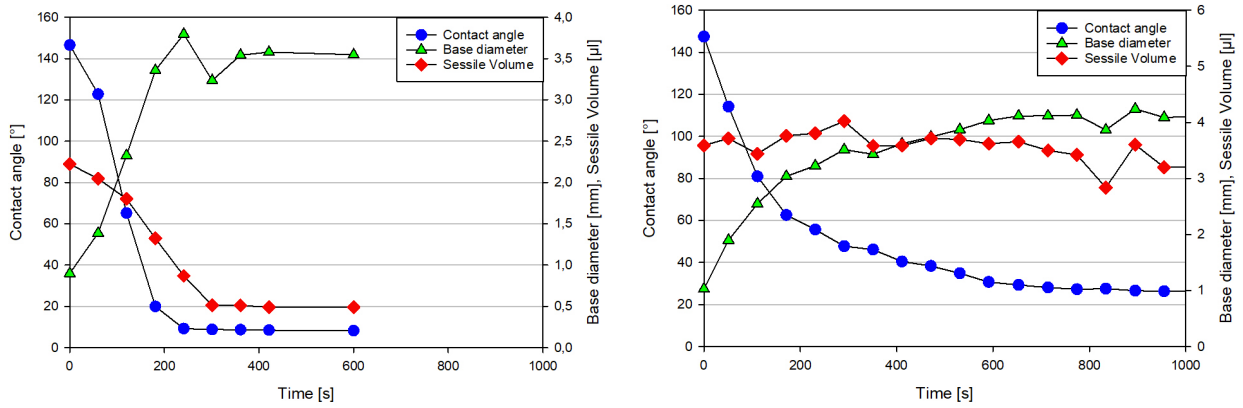

(a) Pure TiB_2 (b) 15wt% C

Figure B.1: Contact angle, base diameter and sessile volume from all the Sessile Drop experiments

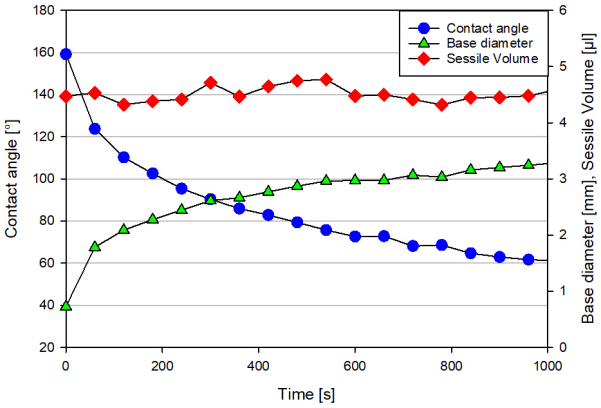

(c) 25wt% C

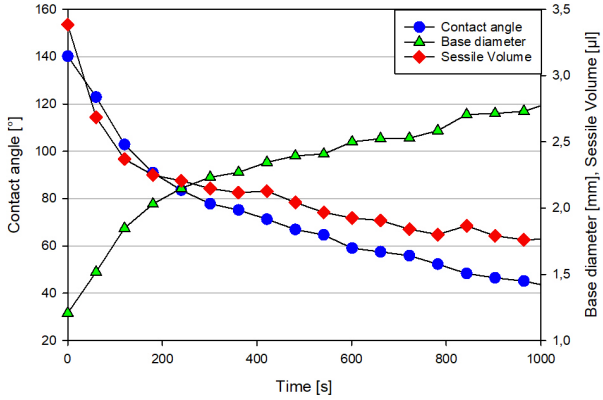

(d) 35wt% C

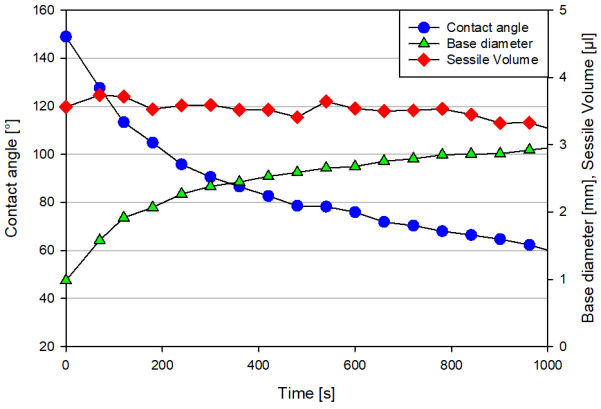

(e) 45wt% C

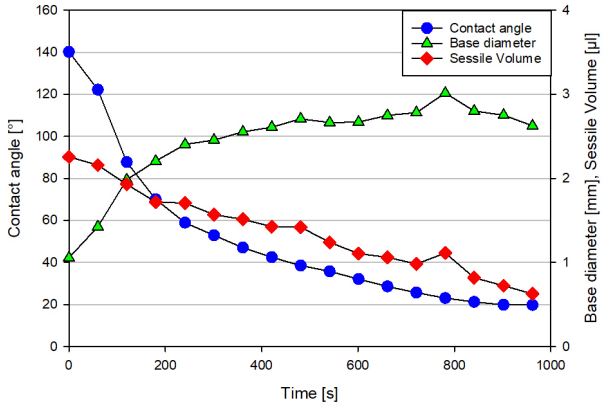

(f) 55wt% C

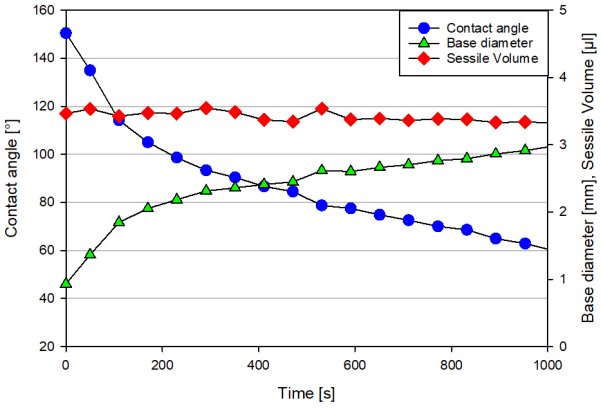

(g) 65wt% C

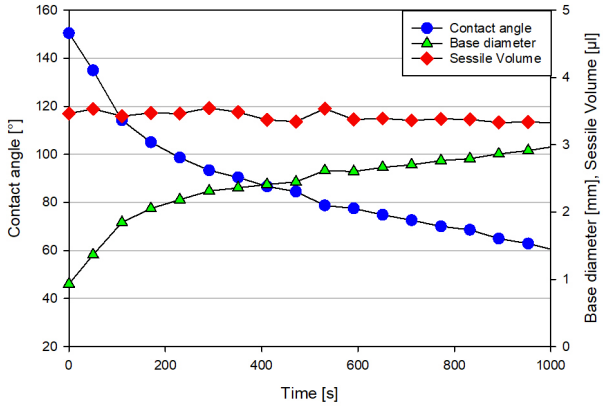

(h) 75wt% C

Figure B.1: Contact angle, base diameter and sessile volume from all the Sessile Drop experiments

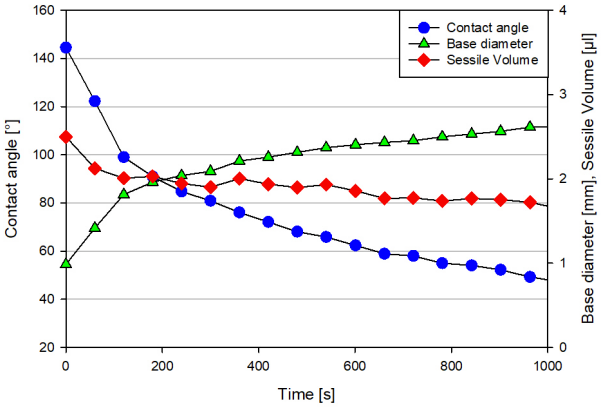

(i) 85wt% C

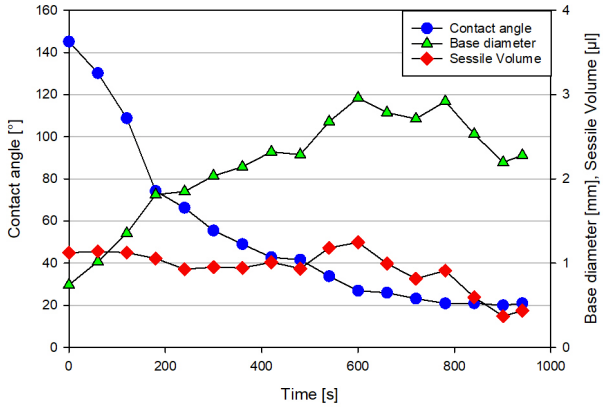

(j) Graphite

Figure B.1: Contact angle, base diameter and sessile volume from all the Sessile Drop experiments

C. SEM Images of the Microstructure

The microstructure of all the sintered samples are shown in Figure C.1. The microstructure of the composition with 55wt% C shown in Figure C.1f has a very different microstructure than the rest of the composites. The reason for this was due to problems during sintering.

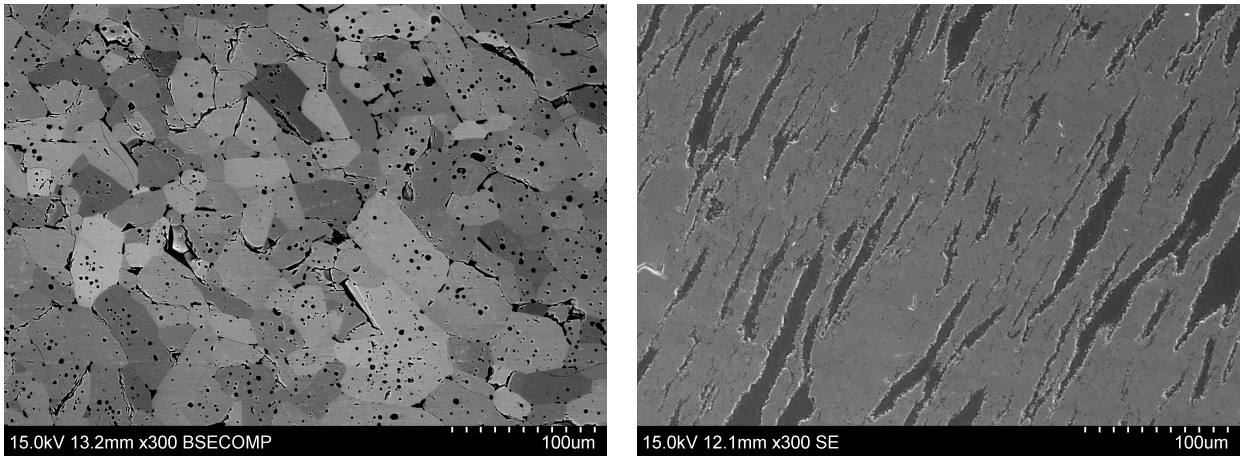

(a) Pure TiB_2 (b) 15wt% C

Figure C.1: SEM images of the different sintered composites including pure TiB_2. All the images are taken at 300x magnification. Image (a) is taken using a BSE detector, the rest is taken using SE detector. The images are of the crossection of the respective samples (image (i) is of the sample surface). The light gray is TiB_2 and the dark gray or black is C.

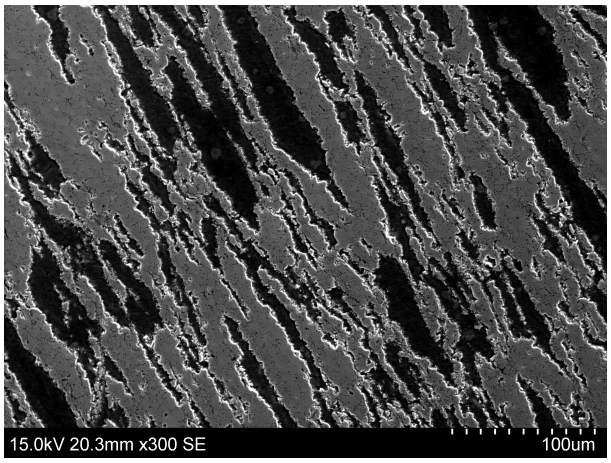

(c) 25wt% C

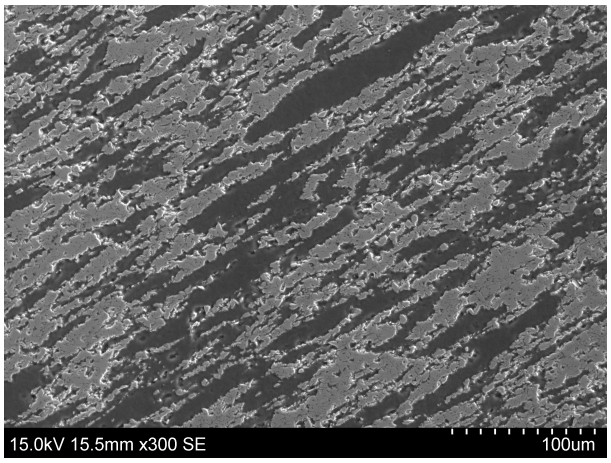

(d) 35wt% C

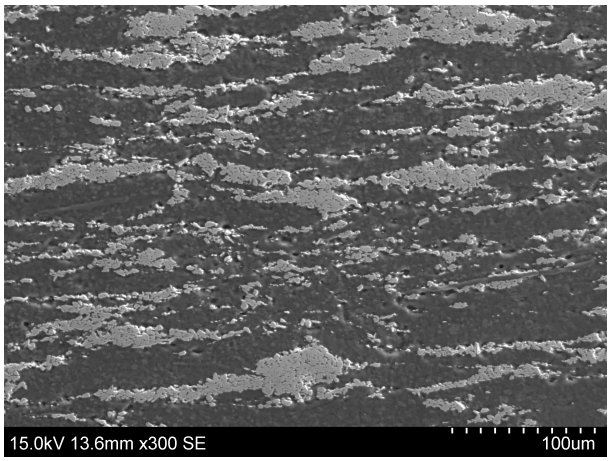

(e) 45wt% C

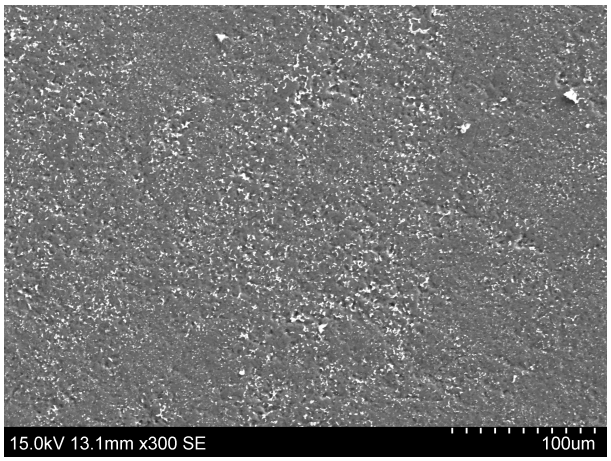

(f) 55wt% C

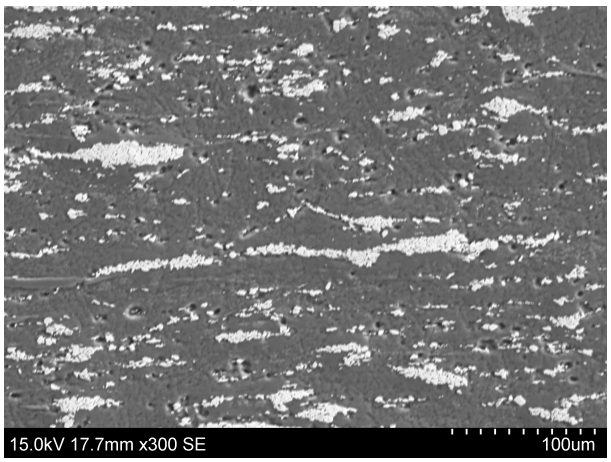

(g) 65wt% C

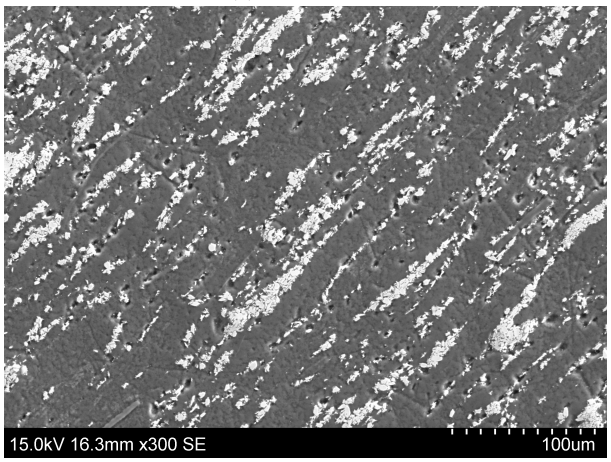

(h) 75wt% C

Figure C.1: SEM images of the different sintered composites including pure TiB_2. All the images are taken at 300x magnification. Image (a) is taken using a BSE detector, the rest is taken using SE detector. The images are of the crossection of the respective samples (image (i) is of the sample surface). The light gray is TiB_2 and the dark gray or black is C.

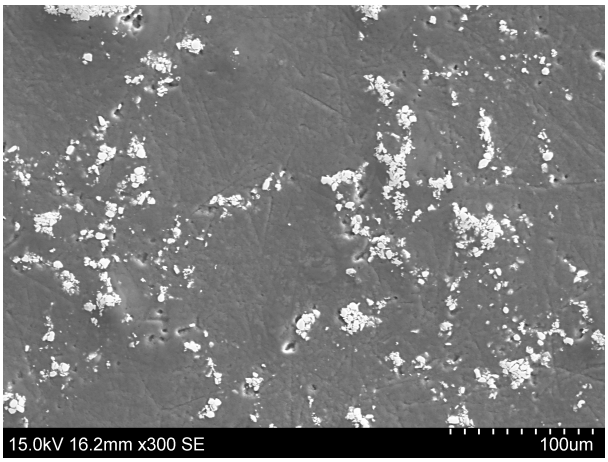

(i) 85wt% C

Figure C.1: SEM images of the different sintered composites including pure TiB_2. All the images are taken at 300x magnification. Image (a) is taken using a BSE detector, the rest is taken using SE detector. The images are of the crossection of the respective samples (image (i) is of the sample surface). The light gray is TiB_2 and the dark gray or black is C.